Struct Bond (2014) 161: 189–242
DOI: 10.1007/430_2013_127

Published online: 13 September 2014

Size- and Ligand-Specific Bioresponse of Gold Clusters and Nanoparticles: Challenges and Perspectives

Janine Broda, Günter Schmid, and Ulrich Simon

Abstract This review gives an introduction to the chemical and physical properties of gold clusters and nanoparticles (NPs) and reflects the present understanding how such particles interact with biological systems in vitro and in vivo. It will acquaint the reader with the basic principles of interaction from a chemical point of view and illustrates perspectives that arise for the application of gold nanoparticles (AuNPs) in biological environments.

Keywords Diagnostics · Gold nanoparticle · Ligand · Nanotoxicity · Size effect · Therapy

Contents

J. Broda and U. Simon (✉)
Institute of Inorganic Chemistry, RWTH Aachen University, 52074 Aachen, Germany
e-mail: Janine.Broda@ac.rwth-aachen.de; Ulrich.Simon@ac.rwth-aachen.de

G. Schmid
Institute of Inorganic Chemistry, University Duisburg-Essen, 45127 Essen, Germany
e-mail: Guenter.Schmid@uni-due.de

1 Introduction

The focus of this review article is the discussion of our present understanding of the interaction of gold nanoparticles (AuNPs) with biological materials in vitro and in vivo, called "bioresponse," as well as the illustration of perspectives that arise for the application of AuNPs in biological environments. The often applied definition of "nanoparticle" – namely to consist of species smaller than 100 nm – is, at least from a scientific viewpoint, too simple. The name nanoparticle should be linked with a characteristic change of properties as is, for instance, the case if AuNPs become smaller than approx. 100 nm when their dispersions in sols or liquids spontaneously become violet or red colored due to the surface plasmon resonance (SPR). Two more precise definitions of nanoscience are therefore cited in Sect. 2.

A prerequisite to understand bioresponse processes is a fundamental knowledge of the influence of size, shape, and surface constitution of the particles. As will be discussed in detail in Sect. 2, the size of a particle is the most important factor influencing predominantly its electronic structure. A gold particle, small enough to restrict the mean free path of the electrons, behaves significantly different from bulk gold. This effect is called "size quantization," saying that such species no longer follow classical physical laws but instead they obey quantum mechanical rules, traditionally used to describe the electronic nature of atoms and molecules. Metal NPs in general and AuNPs in particular have to become very small to reach that state, usually smaller than 2 nm. A prominent example is the Au_{55} cluster (the expression cluster is generally used for NPs with an exact chemical formula, see also Sect. 2) with a diameter of 1.4 nm. It exhibits size quantization properties even at room temperature, whereas larger particles reach this state only at very low temperatures and smaller clusters exhibit discrete electronic states of molecular orbitals. Examples are $[Au_{39}(PPh_3)_{14}Cl_6]Cl_2$ [1], $[Au_{14}(PPh_3)_8(NO_3)_4]$ [2], $[Au_{13}(PR_3)_{10}Cl_2]^{3+}$ [3], or $Au_{11}(PR_3)_7X_3$ [4–6] (X = halogen, thiolate).

The extraordinary position of Au_{55} in the transition range between molecule and extended solid has frequently been demonstrated by its physical properties. Among others, it exhibits quantized charging effects associated with adding an extra electron to a small capacitance, which give rise to applications as a single electron switch at room temperature. Apart from its electronic properties, Au_{55}, usually represented in a ligand-protected version, namely $Au_{55}(PPh_3)_{12}Cl_6$, has a second extraordinary feature: its stability. As will also be discussed in more detail, Au_{55}

is the second of the series of the so-called "full-shell clusters." It consists of a hexagonal close-packed structure like bulk gold and has a cuboctahedral shape. Full-shell clusters follow the composition $10\,n^2 + 2$ for the number of atoms in the nth shell. Particles following this rule are especially stable, as has been demonstrated in a variety of ways. The stability of AuNPs has indeed an important influence on bioresponse, because of the interaction mechanisms between NP and the relevant biosystems. As ligand-free AuNPs cannot be used because of their instability, only ligand-protected species are used. The interaction with any kind of biomolecule and the metal core can only happen, if the original ligands are either completely or at least partially released or replaced during the chemical processes. This means that the protecting ligand shell must have a special nature. If ligand molecules are not sufficiently labile to be removed from the particle's surface, the interaction between the particle and the biological environment only occurs via the protecting skin and not by the metal itself. Phosphine ligands in combination with gold usually fulfill these conditions. $Au_{55}(Ph_2PC_6H_4SO_3Na)_{12}Cl_6$, a water-soluble derivative of the original compound $Au_{55}(PPh_3)_{12}Cl_6$, therefore plays the dominant role in this article. Larger and smaller particles are introduced for comparisons as well as to highlight the emerging field of applications for AuNPs in diagnostics and therapy.

Size, stability, and electronic properties indeed determine bioresponse: Sect. 3 illustrates in vitro applications by discussing the interaction of AuNPs with proteins and cells. While these applications utilize the size-dependent properties of AuNPs as an analytical probe, the molecular mechanisms occur in the ligand shell of the molecules. In contrast 1.4 nm-sized Au_{55} with its weak-binding phosphine ligands turned out to be very cytotoxic. This is demonstrated in series of tests with human cancer cell lines. Two reasons for the cytotoxicity have been proposed: (1) the size of the 1.4 nm Au_{55} clusters fits perfectly to the height of the major grooves of DNA (1.3–1.5 nm) and thus may block transcription of DNA and (2) it induces the formation of reactive oxygen species (ROS) as a consequence of its electronic properties, leading to oxidative damage of neighbored biomolecules and subcellular units. Comparisons with smaller and larger AuNPs, decorated with the same ligand molecules like Au_{55}, clearly show a much less or even no toxicity, supporting the assumption that Au_{55} has a very special bioresponse.

Properties of AuNPs in vivo are introduced in Sect. 4. These experiments inform about distribution in a living body (exemplified by means of rat data), of course depending on the kind of administration. Again, size dependency plays the dominant role. Among a series of AuNPs from 1.4 up to 200 nm, only the 1.4 nm Au_{55} species distribute in all relevant organs, whereas larger particles are accumulated up to 97% in the liver. A further aspect of interest is the role of surface charge in relation to biodistribution experiments with positively and negatively charged 2.8 nm Au particles show little differences. Positively charged species are somewhat less assembled in the liver than negatively charged particles. Furthermore, a new model system for in vivo analyses, i.e., the zebrafish, is introduced with its potential to analyze the properties of AuNPs in whole animal tests.

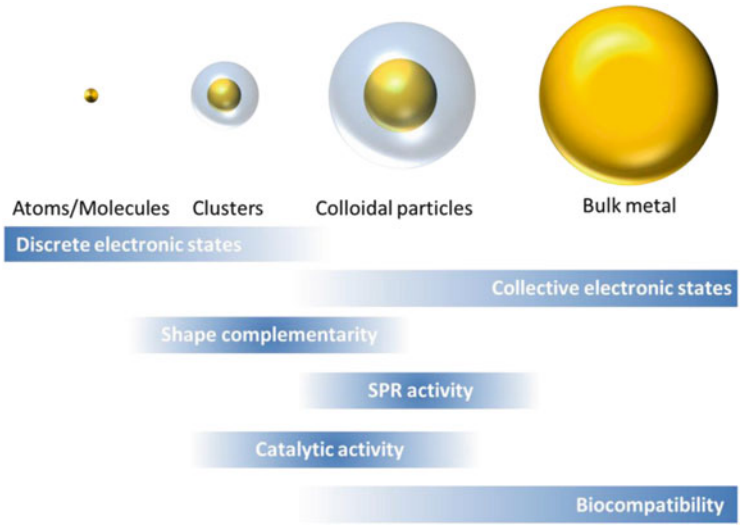

Fig. 1 Schematic presentation of the size-dependent properties of gold, spanning the size range from individual atoms via ligand-stabilized clusters and colloidal particles up to macroscopic bulk metal. The shaded areas indicate size ranges, where specific properties and features of gold occur. Atoms, molecules, and molecular clusters exhibit an electronic structure with discrete electronic states, while colloidal particles as well as bulk gold exhibit collective electronic states. In the size range of clusters and colloids, biological effects may occur due to complementarity in shape to biomolecules and cellular subunits. In this size range the surface plasmon resonance (SPR) dominates the optical properties and most of the size-dependent catalytic properties of gold nanoparticles occur. The biocompatibility increases with sizes above the typical cluster size. The marked areas are not drawn to scale

The final section of this article (Sect. 5) deals with perspectives and challenges of the above findings especially in medicine. Diagnostic and therapeutic aspects as well as drug delivery systems are already partially realized or can be prognosticated (Fig. 1).

2 Size-Dependent Properties of Metal Nanoparticles

The physical and chemical properties of defined materials, for instance elements or chemical compounds in the solid state, depend on size and shape of the particles under consideration. The size dependency of the properties usually becomes obvious in the nanometer regime. Nanotechnology is based on such effects which can have very different appearance. Whereas the bright color of bulk gold is based on relativistic effects [7–9], the red, purple, and blue color of gold nanoparticles (AuNPs) in the size regime of ca. 15 and 50 nm is based on the so-called surface

plasmon resonance (SPR). It is quantitatively described by the Mie theory [10]. The reason for the SPR is to be seen in a size- and shape-dependent collective electron oscillation by interaction with visible light. SPR for copper, silver, and gold is in the visible region and superimposes the relativistic effect, covering the typical color of bulk metals. For other metals it appears in the UV region and is therefore not observable with the naked eye.

Numerous other size effects such as changes of melting points, characteristic magnetic properties, and electronic behavior or the kind of interaction with other species are known and play dominant roles in what we call "nanotechnology." One definition of nanotechnology, considering these different effects, is the following [11]:

> Nanotechnology comprises the emerging application of Nanoscience. Nanoscience deals with functional systems either based on the use of subunits with specific size-dependent properties or of individual or combined functionalized subunits.

The so-called scaling effects, i.e., continuous changes of properties during downsizing a material, are excluded because nano-effects appear only below distinct sizes, resulting in properties which characteristically differ from the macroscopic counterparts. Another similar definition, given by the Royal Society and the Royal Academy of Engineering, also considers the use of molecules and macromolecular systems [12]:

> Nanoscience is the study of phenomena and manipulation of materials at atomic, molecular and macromolecular scales, where properties differ significantly from those at a larger scale. Nanotechnologies are the design, characterization, production and application of structures, devices and systems by controlling shape and size at the nanometre scale.

These definitions include the development of molecular motors and machines, molecular switches, single-electron memories, and, especially considered in this review article, the interaction of metal nanoparticles with biological systems. Why are size-dependent physical and chemical properties decisive for interactions with biosystems and responsible for bioresponse? These connections shall be briefly discussed in this section.

A single metal atom is not a metal in a classical sense. A huge number of atoms are necessary to reach the metallic state, for instance electric conductivity or metallic luster. Corresponding questions arise for other solid elements, for instance silicon. A single Si atom is not a semiconductor. The basic question therefore arises, namely how many atoms are necessary to reach the metallic state and what happens on the way to this state? In spite of various theoretical calculations, numerous experimental results during the last two to three decades have given us some fundamental answers.

The electronic situation in an atom or molecule is best described by following quantum mechanical rules (size quantization). Bulk systems consisting of an infinite number of atoms can widely be described by the laws of classical physics for bulk materials, based on the statistics of infinite numbers of electrons. Figure 2 illustrates the stepwise transition from a three-dimensional (3D) piece of metal (a) via a two-dimensional quantum well (2D) (b), a quantum wire (1D) (c), and

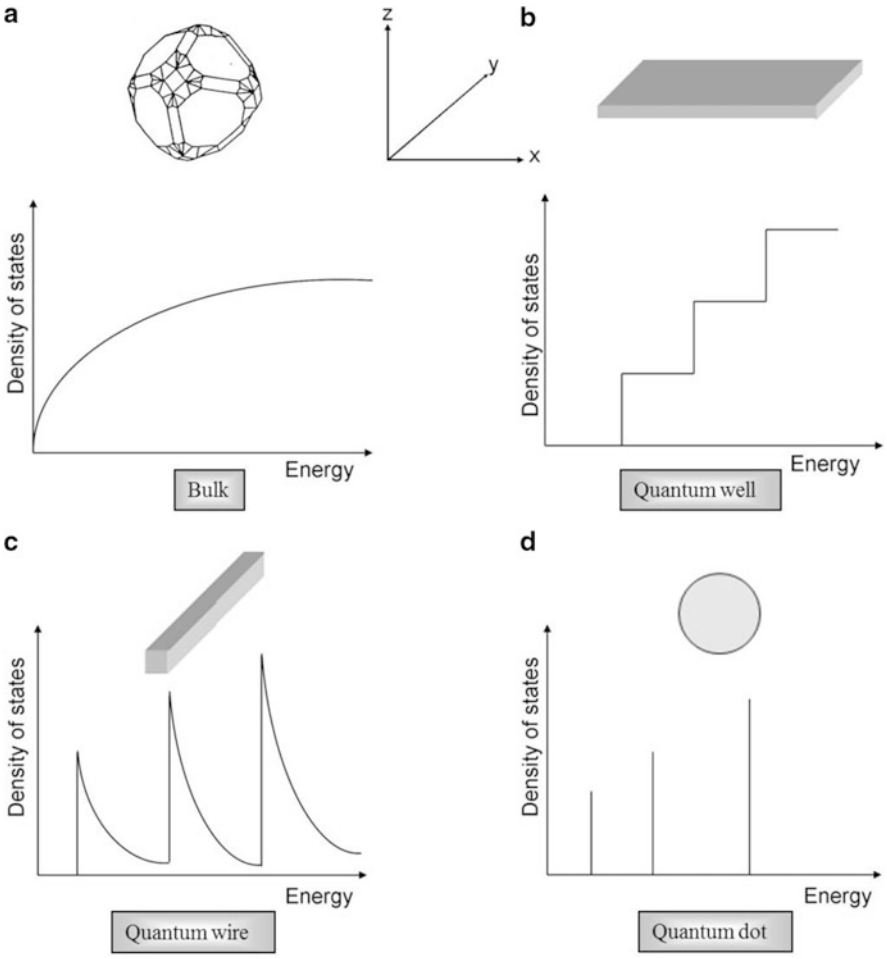

Fig. 2 Transition from a three-dimensional (3D) particle to a 0D quantum dot, correlating with the continuous discretion of the energy states

finally a quantum dot (0D) (d), considering the relation between the density of states and the energy.

On the way from a 3D system to a 2D quantum well, the relation between density of states and energy develops steps, spikes on the way to a 1D quantum wire and, finally, when small enough (0D), discrete energy levels characterize the relationship like in an atom or molecule. The development of a 0D quantum dot can formally also be considered by downsizing a metal particle as is indicated in Fig. 3.

The continuous energy band of s- and d-electrons in the bulk state (a) splits off when the particle is small enough (b, large cluster/nanoparticle) and forms

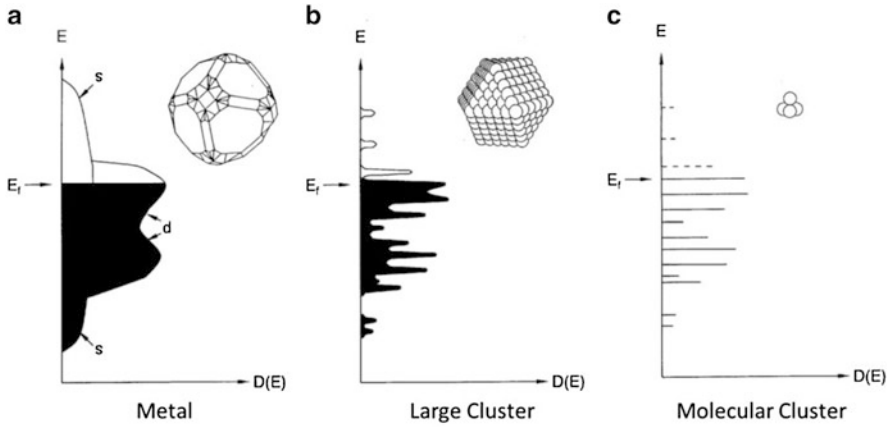

Fig. 3 Sketch of the transition from a metallic bulk state (**a**) via a large cluster (**b**) to a small molecule (**c**) indicating the changes of the electronic situations

sharp energy levels when a molecular cluster[1] is reached (c). What are the experimental results?

The most relevant physical method for investigating individual metal clusters and nanoparticles electronically is to determine the current (I) voltage (U) characteristic using a scanning tunneling microscopy (STM) tip to contact an individual particle on a conductive surface via the obligatory ligand shell. With this technique, single-electron transitions (SET) between tip, particle, and substrate can be observed, if some conditions are fulfilled. The nonconducting protecting ligand shell plays an important role, since neither the STM tip nor the conductive substrate touches the particle itself. SET can only be observed if the electrostatic energy $E_C = e^2/2C$ (C = capacity) is very large compared to the thermal energy $E_T = k_B T$ (k_B = Boltzmann's constant). Since $C = \varepsilon\varepsilon_0 A/d$ (ε = dielectric constant, ε_0 = electric field constant, d = distance of electrodes from metal core, A = surface area), the thickness of the ligand shell is important for the value of C. At very low temperatures single-electron transitions can be observed using rather large nanoparticles. For instance, the I–U characteristic of a 15 nm Pd particle, protected by a shell of $H_2NC_6H_4SO_3Na$ molecules and investigated at 295 K, clearly shows bulk properties, i.e., a linear I–U relationship following Ohm's law. However, at 4.2 K a so-called Coulomb blockade (CB) occurs, indicated by an interruption of conductivity between −55 and +55 mV by a single electron [13]. Figure 4 shows the I–U characteristics at both temperatures.

[1] The difference between the expression "cluster" and "nanoparticle" is not sharp. In the following we will use "cluster" for particles of a discrete number of atoms, whereas "nanoparticle" is used for less exactly defined species, allowing a certain size distribution.

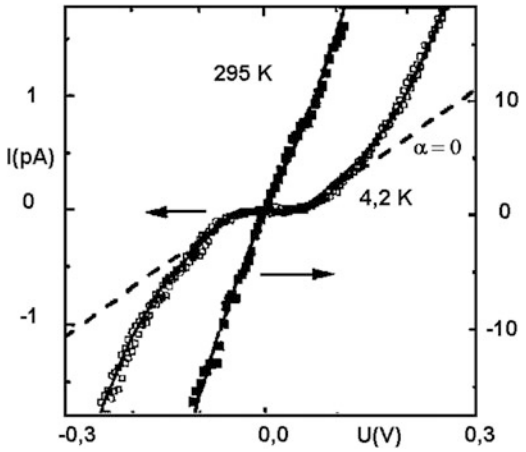

Fig. 4 Current (I)–voltage (U) characteristic of a ligand-protected 15 nm Pd particle at 295 K and 4.2 K. Ohm behavior is observed at 295 K, whereas a Coulomb blockade is existent at 4.2 K. Figure reprinted with kind permission from [13]

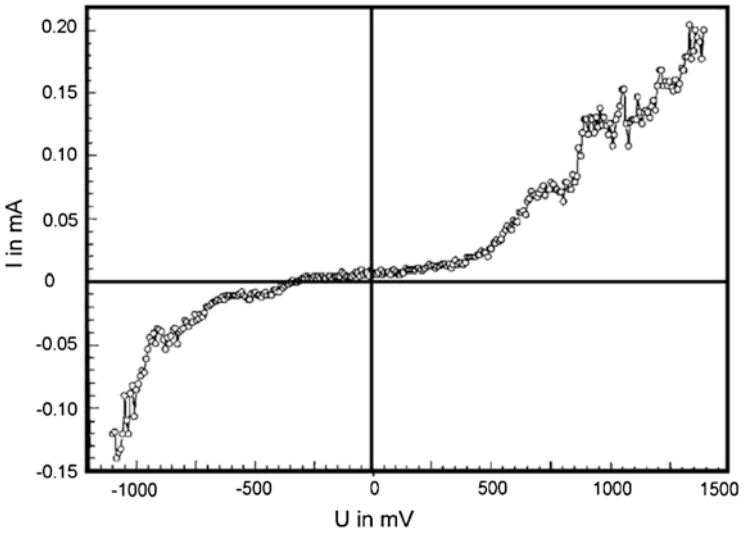

Fig. 5 I–U characteristic of Au_{55} $(PPh_3)_{12}Cl_6$ at 295 K exhibiting a well-expressed Coulomb blockade between −500 and +500 mV. Figure reprinted with kind permission from [15]

Of course, the existence of nanoparticles showing a Coulomb blockade already at room temperature is of high interest for future applications, for instance, as single electron switches. Indeed, such a particle (cluster) has been found with $Au_{55}(PPh_3)_{12}Cl_6$ [14]. The diameter of the Au_{55} core is only 1.4 nm. The I–U characteristic of an individual cluster clearly exhibits Coulomb blockade at 295 K between −500 and +500 mV as can be seen in Fig. 5 [15].

The Au_{55} cluster has another special property: it belongs to the so-called very stable full-shell clusters, species having an icosahedral or a hexagonal close-packed cuboctahedral shape, consisting of a distinct number of atoms per shell around 1 central atom, namely $10n^2 + 2$ atoms (n = number of shell). The smallest full-shell Au cluster with $n = 1$ consists of 1 + 12 atoms, well known since 1981 with icosahedrally structured Au_{13} cores [3, 16]. Numerous full-shell clusters of other metals have become known in the meantime, for instance the four- and five-shell clusters Pt_{309} [17] and Pd_{561} [18]. Whereas the ligand-protected Au_{13} cluster has still typical molecular properties, the Au_{55} species is just at the borderline between molecule and bulk and is therefore often called as "metal in the embryonic state."

The answer to the aforementioned question, why electronic and structural properties of clusters or nanoparticles are of relevance with respect to bioresponse, is not very surprising. First of all, the stability of metal particles in a biological medium is of high importance because less stable species would decompose, forming smaller or larger species with different properties. So, a stability guaranteeing structure and size is a condition for reliable results. The electronic structure is responsible for the chemical activity of a particle and so influences fundamentally the interactions with other materials. Some examples of these two factors are given.

Au_{55} and various smaller and larger gold nanoparticles and even bulk gold surfaces have been investigated with respect to their activity against oxygen in an oxygen plasma by means of X-ray photoelectron spectroscopy (XPS) [19]. Except Au_{55}, all other species became partially or quantitatively oxidized! Why not Au_{55}? This is because of its structure. Oxidation of the cuboctahedral structure would afford too much energy so that oxidation, even under the exceptional conditions in an oxygen plasma, does not happen.

The special stability of the Au_{55} nucleus becomes additionally visible when again AuNPs, smaller and larger than Au_{55}, are contacted with indium vapor. Bulk gold forms an alloy of the composition $AuIn_2$. All other NPs react easily with In vapor, but again not Au_{55}. It remains unreacted [19].

Theoretical [20] and experimental results [21] show that very small AuNPs are most active in oxygenation catalysis. Especially particles below ~3.5 nm are the most active species, indicating that electronic properties play a decisive role in chemical processes. $Au_{55}(PPh_3)_{12}Cl_6$ with a core diameter of 1.4 nm, supported on inert materials, turned out to be the most active catalyst for the selective oxidation of styrene by dioxygen [21]. In this case, particles larger than ~2 nm are completely inactive. This finding is of high importance considering the cell toxicity of Au_{55} species due to oxidative stress (reactive oxygen species, ROS) [22]. Though larger AuNPs also cause oxidative stress, the 1.4 nm cluster is the most active particle. Oxidative stress is caused by activation of dioxygen when touching the metal surface however, without oxidation of Au atoms. Details will be given in Sect. 3.

Another result indicating the special role of Au_{55} clusters shall briefly be mentioned. It is the relaxation behavior of excited electrons, compared with two other particle sizes [23]. If 0.7 nm (Au_{13}), 1.4 nm (Au_{55}), and 15 nm AuNPs are

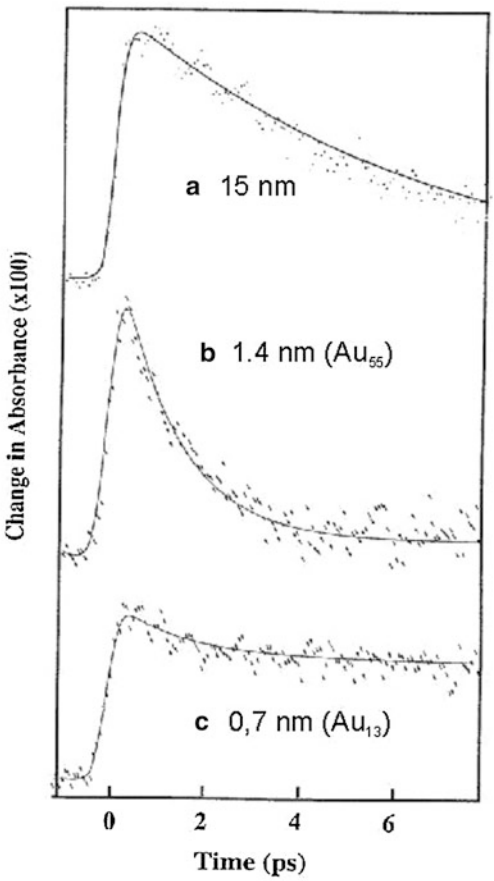

Fig. 6 Relaxation behavior of excited electrons in three differently sized AuNPs. Figure reprinted with kind permission from [23]

treated by femtosecond laser pulses, the corresponding relaxation times are size dependent. They are very different between Au_{55} and the other two species. The relaxation time is dependent on the electron–phonon coupling and the electron surface collision. In larger particles it is dominated by the weakening of the electron–phonon coupling, resulting in a slowdown of the relaxation. On the way from 15 to 1.4 nm, electron surface collision increases and consequently the relaxation time decreases. On the other side, the 0.7 nm Au_{13} cluster behaves molecular-like due to the fixed electrons between the Au atoms. Its relaxation is very slow. These results impressively demonstrate Au_{55} clusters to behave like species just one step before molecular and one step behind metallic state. These correlations can be followed from Fig. 6.

Up to here, we have discussed the influence of size, structure, and electronic properties on the relevance concerning bioresponse. However, there is another, very important factor: the protecting ligand shell. As already mentioned above, the use

of bare metal clusters and nanoparticles is not possible. Prevention of coalescence affords a "skin" of appropriate molecules on the particles' surface. The chemical nature of protecting molecules determines not only the solubility in different solvents, but it is decisively responsible for the initial contact between the particle and, in our case, a biosystem. For instance, $Au_{55}(PPh_3)_{12}Cl_6$ is only soluble in polar organic solvents and can therefore not be used for experiments in living systems. Therefore, a derivative with hydrophilic phosphine ligands is used, namely $PPh_2C_6H_4SO_3Na$ (monosulfonated triphenylphosphine, TPPMS) [24]. The "skin" determines what first happens. This fact can be used for surface recognition or specific targeting [25]. The specific nature of the metal particle becomes only effective if all or at least part of the ligand molecules are removed. Phosphines, coordinated to Au atoms, indeed fulfill this condition as has been shown by ^{31}P NMR studies [26] and as can be followed from the different results with respect to bioresponse, as will be demonstrated later. The cell toxicity of $Au_{55}(PPh_2C_6H_4SO_3Na)_{12}Cl_6$, discussed in more detail in Sect. 3, can clearly be traced back to the Au nucleus itself, since the phosphine ligands have been found to be nontoxic. If the easily removable phosphines are substituted by stronger coordinating thiols, the toxicity of the Au_{55} clusters is suppressed, since contacts between the clusters and the corresponding cell components happen only via the nontoxic end-groups of the thiols (e.g., glutathione, GSH) [22]. Living cells contain numerous different potential "ligands" that can substitute part or all of the original phosphines and then are directly in contact with the active Au_{55} cluster core. Unfortunately, these important relations between ligand-protected metal nanoparticles and any other system under investigation are often not sufficiently considered in the literature [27–29].

3 In Vitro Applications: Interaction with Proteins and Cells

AuNPs in general have attracted considerable interest for applications in vitro and in vivo. Since for most applications the particles' size is in the range of 10–20 nm and stabilizing ligands are thiols, they are typically considered nontoxic, and together with the relatively low amounts, which are applied for different purposes either in vitro or in vivo, it seems to be unlikely that AuNPs cause environmental pollution or health risk due to unintended exposure. Nevertheless, ultrasmall AuNPs can interact with cells and can induce cell death via different pathways, which is related to the size but also to the surface functionalization, as described above. The next two sections will shed light on the state of knowledge about the properties and applications of different classes of nontoxic AuNPs in vitro by means of selected examples. In these examples the AuNPs serve as a scaffold for the binding of (bio)molecules in in vitro applications so that the properties are determined by the binding molecules and by the particle itself. However, the

nanoscale features of the AuNPs, e.g., self-fluorescence or SPR, are utilized as probes to study the interaction with biomolecules. These two chapters will be followed by a chapter on in vitro studies on cytotoxic AuNPs, in particular of the 1.4 nm AuNPs, where the gold core itself is biologically active.

3.1 Interaction with Proteins: The Corona Effect

The functionality and bioactivity of AuNPs in biological fluids and in particular in cells are critically dependent on the dispersion state. While in well-dispersed AuNPs the properties of the individual particles are retained, aggregating nanoparticles will progressively approach the properties of micron-sized or even bulk material. For any kind of application, it is vital to control the interaction between the AuNPs and the biomolecules in their respective environment, which can cause aggregation and severe change in the surface properties of the nano-objects and, hence, affect their (hydrodynamic) particle size, surface charge, uptake mechanism, intracellular trajectory, and even the toxicity profile.

The most prominent protein which has been studied in its interaction with NPs of different sizes and composition is serum albumin, which is the most abundant globulin in serum. Due to its negative gross charge, it electrostatically binds to positively charged AuNPs, e.g., particles carrying a terminal amine group, and can overcompensate the particle charge turning it from positive to negative. This binding is associated with an increase of the hydrodynamic radius and enhances reabsorption of the AuNPs in tubules via the neonatal Fc receptor–albumin binding.

The nanoparticle protein-binding kinetics has been analyzed by means of several methods, which probe either fluorescence quenching or fluorescence enhancement of the AuNPs [30, 31]. It was shown that the fluorescence from tryptophan, tyrosine, and phenylalanine residues in proteins was quenched upon binding to the AuNP, which indicates a conformation change of the protein. This allowed analysis of the binding kinetics and the analysis of size effects. It turned out that ultrasmall AuNPs exhibit different binding affinities compared to larger ones. For sub-2 nm AuNPs even the strong self-fluorescence emission at 684 nm could be utilized to analyze the interaction with human serum albumin (HSA) protein, apo-transferrin, lysozyme, and apolipoprotein E4. A signal enhancement was observed upon protein adsorption with increasing concentration of the protein (cf. Fig. 7). Since these four proteins do not exhibit any fluorescence in this spectral range, it is assumed that binding of the proteins slows down the fluorescence decay rate and by this enhances the fluorescence signal intensity of the AuNPs by reducing the polarity of the local environment.

This is one example how the formation of a “protein corona” surrounding an AuNP can be analyzed, and it might be assumed that this process will occur either on the surface of the protecting ligand shell of the particles or directly on the particle surface, when weak-binding ligands, such as TPPMS, are replaced by

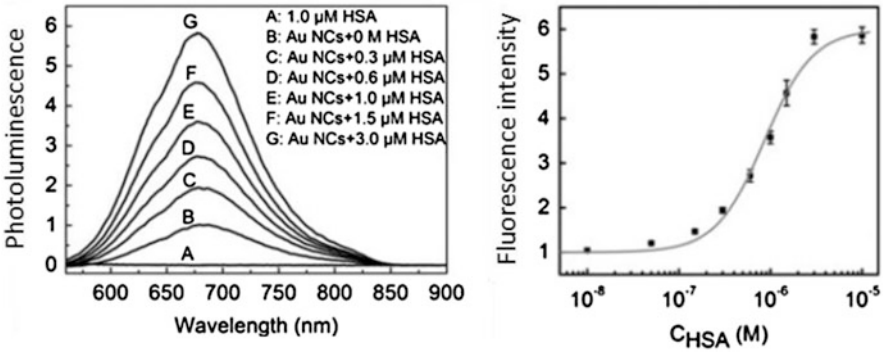

Fig. 7 *Left*: Photoluminescence spectra of HSA (curve *A*) and sub-2 nm AuNPs in the presence of different concentrations of HSA (curves *B–G*), taken with excitation at 550 nm. *Right*: Fluorescence intensity of these AuNPs, plotted as a function of the HSA concentration in the solution. The gray line fits to the data points using the adapted Hill equation. Figure adapted from [30]

stronger binding or multivalently coordinating molecules. Nevertheless, the mechanistic details of this interplay between AuNPs and proteins are still rather unexplored. A very recent review by Treuel and Nienhaus gives a comprehensive overview about the state of knowledge and the challenges in this particular field of nanoparticle research [32].

3.2 *Biofunctionalized Particles: Examples for In Vitro Applications*

A very robust form of functionalized AuNPs for application in vivo has been introduced by Mirkin and his group [33–48]. A very recent research perspective gives an excellent overview about the features and perspectives arising from this technology and shall briefly be summarized [49]. They introduced and intensively studied the assembly induced shift of the surface plasmon resonance (SPR) for the detection and sensing of nucleic acids. In this process AuNPs are functionalized with oligonucleotides via terminal thiol groups. These AuNPs, also described as spherical nucleic acids, possess designed recognition properties encoded by the nucleic acid sequence of the respective oligonucleotide ligands. Based on bases sequence complementarity of the oligonucleotides, either direct particle–particle hybridization or assembly via linker strands becomes possible. Hence, in a solution mixture of two kinds of AuNPs with noncomplementary base sequence, addition of a target DNA that is complementary to both sequences of surface-bound DNA (linker strand) will induce AuNP aggregation due to the binding to both kinds of AuNP via DNA hybridization (Fig. 8).

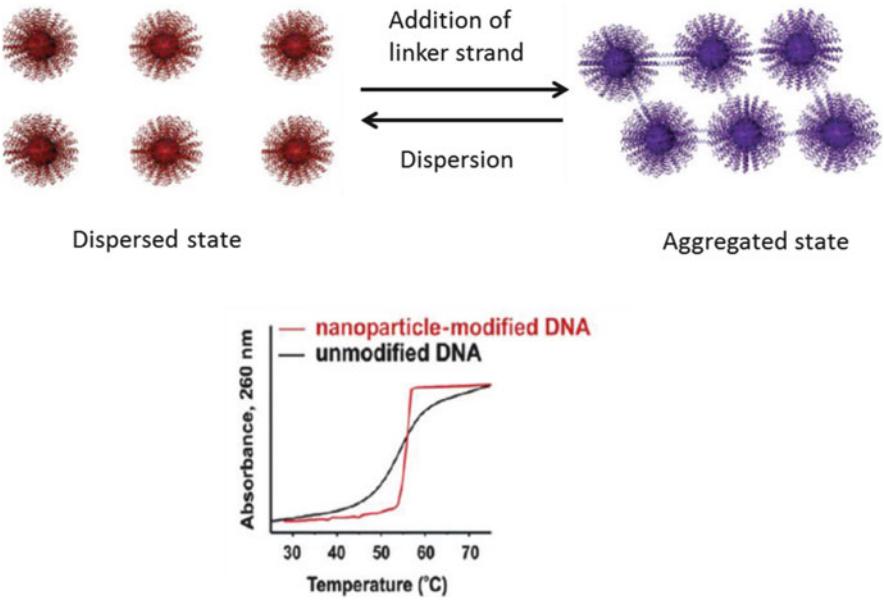

Fig. 8 *Top*: Schematic illustration of the aggregation and dispersion of DNA−AuNP conjugates. The corresponding SPR shift is indicated by the color of the AuNPs. The solution of dispersed particles appears red, whereas aggregated particles turn the samples purple. Aggregation can be induced via linker strands (as shown here) or by metal ions or any molecule that the oligonucleotide shell has been programmed to recognize and bind. *Bottom*: Compared to duplexes of free-strand DNA, which dissociates over a broad temperature range, the melting transitions of oligonucleotide functionalized AuNPs are sharp and occur over a very narrow temperature range due to the cooperative binding of the nucleic acids in the ligand shells. Figure adapted from [49]

Aggregation, i.e., polymeric macroscopic assembly of the AuNPs, can quite easily be followed by means of a SPR red shift, which causes a change of the solution color from red to blue. Since the aggregation results from DNA linkages, these DNA–NP conjugates can be disassembled through dehybridization of the duplexes via heating or by lowering the solution salt concentration. As it is well known from "free" DNA duplexes, melting dehybridization occurs when the temperature is raised above the melting point (T_m), whereas T_m is predictable by base sequence design. In contrast to "free" DNA duplexes, which exhibit melting transitions over a broad temperature range (~20°C), the melting transition in DNA–NP conjugates occurs over a very narrow temperature range (~2–8°C) and at a temperature higher than the T_m of the particle-free DNA duplex. This reflects cooperative binding in a highly predictable manner, where a single oligonucleotide base-pair mismatch can influence the melting behavior of the aggregate. It was immediately recognized that these striking features could be utilized for high-selectivity detection platforms, which include the quantitative measurement of enzymes, DNA-binding molecules, or bioactive metal ions [50–53].

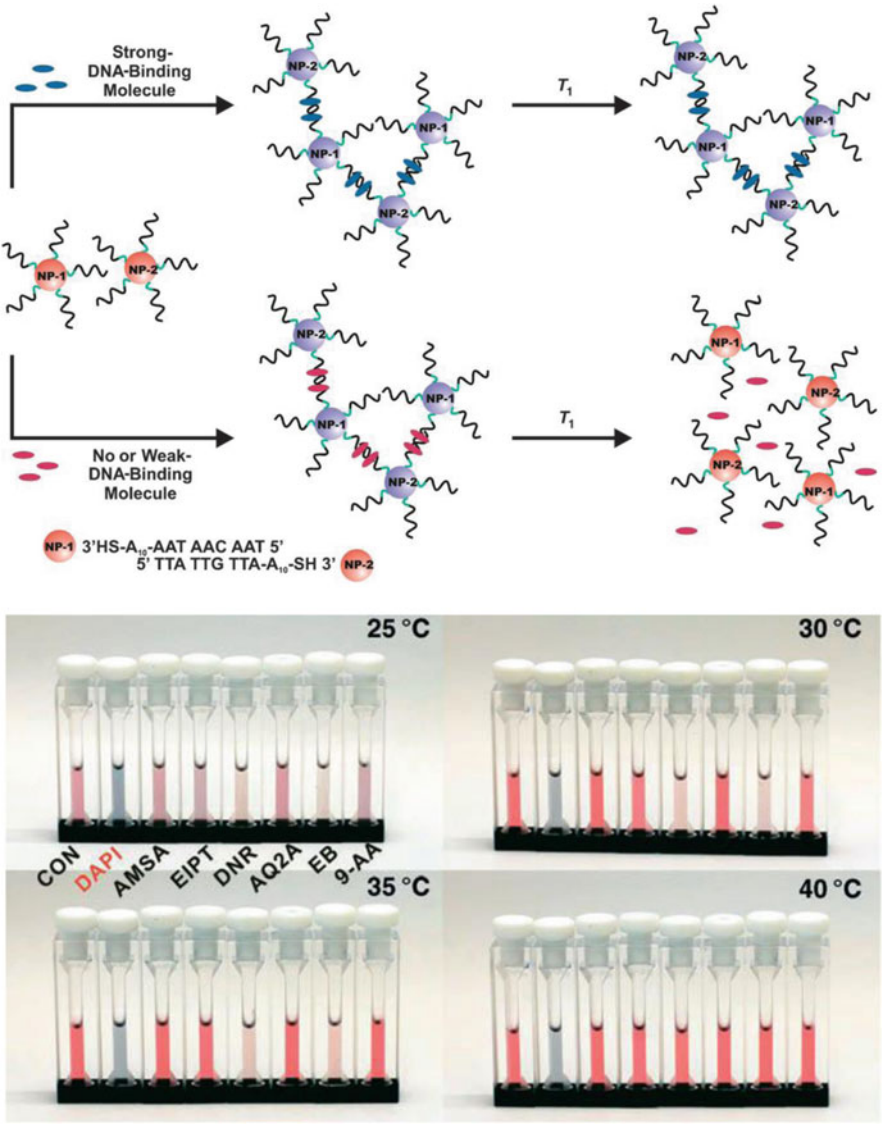

Fig. 9 *Top*: Schematic representation of the structural and color change of nanoparticle/DNA-binding molecule assemblies at a specific temperature (T1). *Bottom*: The color change of the nanoassembly (NP-1 and NP-2, each 1.5 nM) in the absence (CON) and presence of DNA-binding molecule (5 μM)-specific temperatures. Figure reprinted with kind permission from [52]

Figure 9 illustrates a colorimetric screening of DNA-binding molecules with AuNPs functionalized with oligonucleotides [52]. It was developed to determine the binding affinities between potential DNA-binding molecules and duplex DNA in AuNP–DNA networks. The colorimetric readout does not require additional instrumentation, since it relies of the color change via plasmon coupling upon

particle aggregation. When the networks are formed in the presence of duplex DNA-binding molecules, such as DAPI (4′,6-diamidino-2-phenylindole) or EB (ethidium bromide), the resulting duplexes connecting the AuNPs become more stable due to the DNA-binding interactions (p–p stacking, electrostatic, or hydrogen bonding). This increases the melting temperature so that the presence of different DNA-binding molecules can be read out from the temperature-dependent color change.

Based on this fundamental properties of DNA-functionalized AuNPs, Mirkin and others have developed more sophisticated techniques, including chip-based scanometric assays, which have been commercialized partially for highly sensitive molecular diagnostic technologies including clinical disease states, such as Alzheimer's disease or prostate cancer [49]. Furthermore, the unique set of properties is useful for intracellular applications. This includes the high affinity for complementary DNA and RNA [54], the pronounced stability against nuclease degradation [55], and no observed toxicity [56], which allows application as gene regulation agents [57].

Interestingly, despite their large negative charge due to the polyanionic DNA, the AuNP–DNA were found to easily enter cells. It was demonstrated recently that uptake of these particles in tumor cells (HeLa) is mediated by scavenger receptors. Blocking of these receptors with well-known ligands, polyinosinic acid (PolyI) and Fucoidan, has led to inhibition of particle uptake to a high degree, demonstrating competitive binding of AuNP–DNA and the inhibitors to the receptors. The extent of uptake increases with increasing number of DNA ligands per AuNP and is supported by positively charged scavenger proteins. The presence of serum proteins reduced particle uptake as the adsorption of these proteins on the AuNP–DNA is suspected to compete with receptor binding [58]. This suggests that the interactions between AuNP–DNA and scavenger receptors via the scavenger proteins are a charge-mediated process. These unique features hold great promise for applications in gene regulation therapies as well as in diagnostics, since it was shown that also other inorganic particles, in particular iron oxide particles [59] as well as the so-called "coreless spherical nucleic acids," i.e., cross-linked nucleic acids, which are oriented in the same way as in the case of AuNP–DNA but do not carry an inorganic core [57], exhibit the same uptake properties.

Recently, DNA-functionalized AuNPs have been used as a platform to study the interaction of even weaker-binding molecules in a similar colorimetric approach. Witten el al. introduced glyconanoparticles with thermally addressable DNA ligands, i.e., they bound glycomodified oligonucleotides to complementary functionalized DNA–AuNP to form glyco-DNA–gold nanoparticles (AuNP–DNA-glyco) [60]. These particles provide a multivalent presentation of DNA-glyco ligands that assemble as a result of the binding of carbohydrate-binding proteins, the so-called lectins, which carry a carbohydrate recognition domain (CRD). These carbohydrate–protein interactions play an important role in processes such as cell–cell or cell–matrix interactions and are exploited for the design of glyconanoparticles, e.g., for vaccine development or in vivo imaging [61]. In the example given, the coupling of AuNP–DNA with *N*-acetyl-d-glucosamine (GlcNAc)-modified

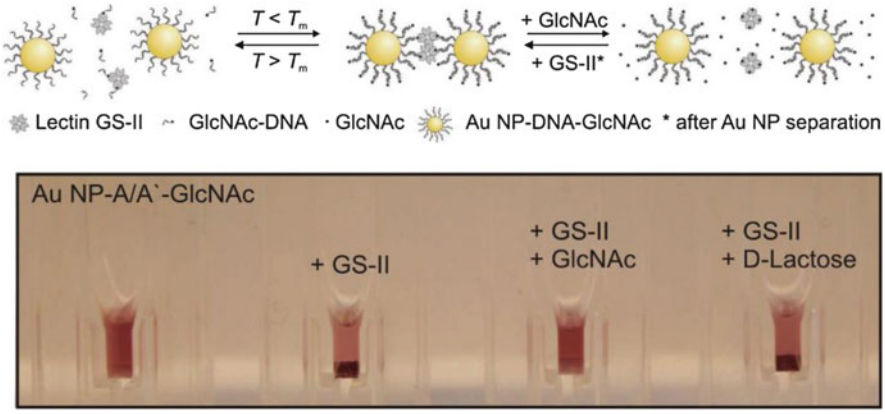

Fig. 10 *Top*: Schematic illustration of the reversible GS-II- and GlcNAc-DNA-mediated assembly of AuNP–DNA. Lectin–DNA–AuNP networks are dissociated by external stimuli: temperature-induced DNA melting or competition with free GlcNAc. After competition with free GlcNAc, the particles are separated by centrifugation enabling reassembly by the new addition of GS-II. Note that the scheme is not drawn to scale. ssDNA refers to single-stranded DNA. *Bottom*: GS-II-mediated assembly of AuNP–DNA-GlcNAc and subsequent competition with GlcNAc or D-lactose. Photographs of the samples: AuNP–DNA-GlcNAc, AuNP–DNA-GlcNAc 2 days after the addition of GS-II, AuNP–DNA-GlcNAc 2 days after addition of GS-II, and subsequent addition of GlcNAc or D-lactose (from left to right). Figure reprinted with kind permission from ref. [60]

single-stranded DNA (DNA-GlcNAc) to form DNA-GlcNAc-functionalized AuNPs (AuNP–DNA-GlcNAc) is demonstrated. The particles assemble in the presence of the tetrameric lectin GS-II with four CRDs with affinity for GlcNAc [62]. Assemblies built up by the GS-II AuNP–DNA-glyco interaction were shown to be equipped with two reversible binding modes that enable the reversible dissociation by two independent external stimuli: temperature-induced DNA duplex melting and displacement of the DNA-glyco ligands from the CRDs of the lectin by competition with free sugar [60] (Fig. 10).

3.3 Interaction with Cells

3.3.1 Cyto- and Genotoxicity

Numerous reports about toxicity and nontoxicity of metal nanoparticles can be found in literature [29, 63–80]. Most of the reports are dominated by results concerning AuNPs. Silver, known for its antibacterial function for more than 100 years, also plays an important role. However, gold absolutely dominates the scene. Silver (15–25 nm), gold (5–6 nm), and silver–gold alloy nanoparticles (10–12 nm), protected either by poly(vinylpyrrolidone) (PVP) or

tris(3-sulfonatophenyl)phosphine (TPPTS), have recently been tested toward human mesenchymal stem cells (hMSC). As expected, AgNPs showed a significant influence on the cell viability in contrast to the AuNPs with only a small effect. Surprisingly, the alloy particles, though containing silver, had no significant influence on the viability of the cells [81]. Most of the numerous reports on bioresponse of AuNPs are characterized by a disadvantage: the conditions of the various studies all differ so that comparisons are difficult to be drawn. First of all, the experiments differ not only by the particles' size and shape but, even more important, by their protecting ligand shell. As has already been discussed in Sect. 2, variations of the particles' skin may change toxicity into nontoxicity or vice versa. Another problem to compare literature data is the use of different cell lines, doses, time of observation, etc. If the metal-specific toxicity is of interest, contact between cell components and metal surface atoms is a condition, but not between ligand molecules and the corresponding biomolecules. Nontoxicity of cystein- and citrate-capped 4 nm AuNPs, glucose-covered 12 nm Au particles, or citrate-, biotin-, and cetylammonium bromide (CTAB)-modified 18 nm particles in human K562 Leukemia cells has been observed [82, 83], whereas toxicity of poly (ethyleneglycol) (PEG)-coated 13 nm AuNPs causes acute inflammation and apoptosis in the liver [27]. A review article with many details describes results of in vitro and in vivo toxicity studies up to 2010 [29].

As already mentioned in Sect. 2, reliable results regarding size dependency can only be gained if identically coated AuNPs are used and which, most importantly, quantitatively or at least partially lose their ligand shell in contact with cell species to allow direct contact between the gold surface and the relevant biomolecules. Phosphines, coordinated to the surface of AuNPs, fulfill this condition.

$Au_{55}(PPh_2C_6H_4SO_3Na)_{12}Cl_6$ has exclusively been applied to study toxicity in a series of human cancer cell lines. Preceding experiments with this cluster compound and B-DNA showed that phosphine molecules are substituted by DNA sections comprising the major grooves. The reason for this result is to be seen in the size conditions: the diameter of the Au_{55} nucleus is 1.4 nm and the height of the major grooves is 1.3–1.5 nm. As molecular calculations of that system showed, there are strong chemical interactions between the Au_{55} core and the DNA, supported by the polydentate character of the major grooves [84]. At least so many ligands are removed from the original cluster that Au_{55} fits into the groove to allow interactions with relevant DNA components. The coverage of B-DNA with Au_{55} clusters has already been supposed by a preliminary experiment, namely when B-DNA in aqueous solution was contacted with the coated clusters and investigated by atomic force microscopy (AFM) [85]. Cross sections show the correct difference in height between unloaded and cluster-containing DNA sections. The observed 1.8 nm sections correspond with the sum of the DNA plus about half of the cluster, possibly still having some ligand molecules outside. Figure 11 shows the AFM image and the cross section indicating the difference between DNA with and without Au_{55} clusters. Figure 12 shows the result of the molecular modeling calculations.

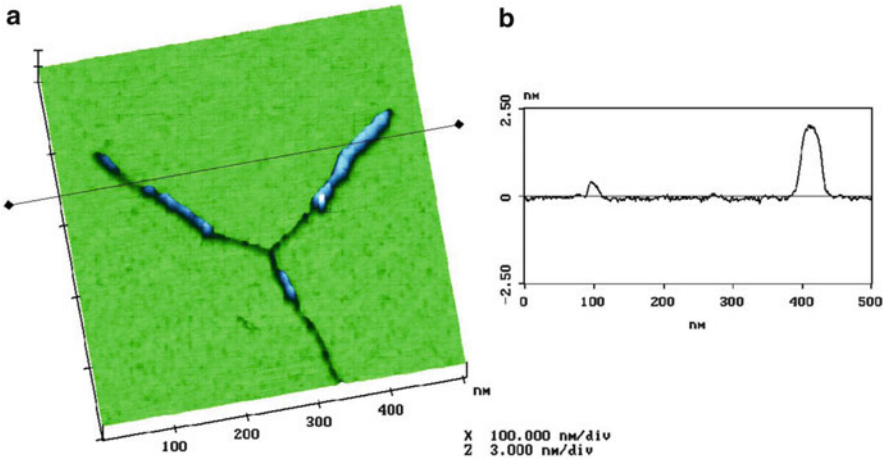

Fig. 11 (**a**) AFM image of DNA sections partially linked with Au_{55} clusters. (**b**) Height profile of unloaded and loaded parts, respectively. Figure reprinted with kind permission from [84]

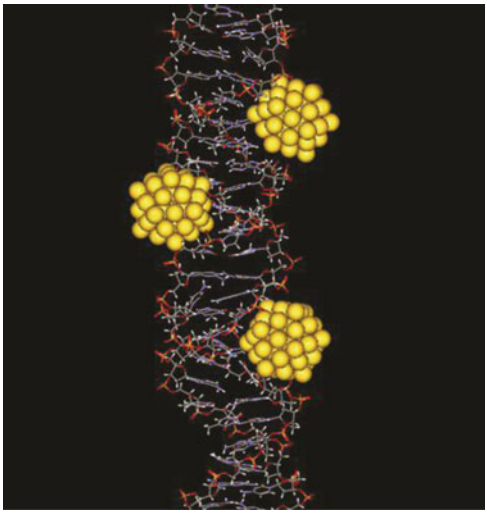

Fig. 12 Energy-minimized structure of B-DNA with Au_{55} clusters along the phosphate backbone of the major grooves. Figure reprinted with kind permission from [84]

The Au_{55} clusters are bound in a stable manner to the major grove of B-DNA as various investigations showed [85].These results clearly indicate that the original phosphine ligands can be removed by biological materials without any problem. An important consequence of this finding is that a DNA, damaged in this manner, can no longer be active in a cell, synonymous with cell death. In other words, 1.4 nm Au_{55} clusters must finally be toxic.

In a series of experiments the toxicity of Au_{55} has been investigated using 11 different types of human cancer cells in comparison with cisplatin, a commonly

Table 1 IC_{50} values of 11 human cancer cell lines treated with cisplatin (72 h) and Au_{55} (24 h). Table reprinted with kind permission from ref. [85]

Cell line		IC_{50} cisplatin 72 h (μM)	IC_{50} Au_{55} 24 h (μM)
MC3T3-E1	Normal bone cells	26.1 ± 1.27	1.65 ± 0.14
U2OS	Osteosarcoma	11.17 ± 2.02	0.64 ± 0.04
SK-ES-1	Osteosarcoma	0.79 ± 0.17	1.03 ± 0.18
MOR/P	Lung cancer cells	3.30 ± 0.3	2.10 ± 0.10
MOR/CPR	Lung cancer cells	7.10 ± 1.2	2.50 ± 0.10
CCD-919Sk	Fibroblast cells	0.45 ± 0.10	0.62 ± 0.07
BLM	Metastatic melanoma	54.70 ± 7.60	0.30 ± 0.10
MV3	Metastatic melanoma	>50	0.24 ± 0.02
SK-Mel-28	Melanoma	15.60 ± 2.26	1.12 ± 0.16
HeLa	Cervical cancer cells	7.93 ± 0.95	2.29 ± 0.10
Hek-12	Kidney cancer cells transfected with adenovirus	20.13 ± 6.0	0.63 ± 0.02

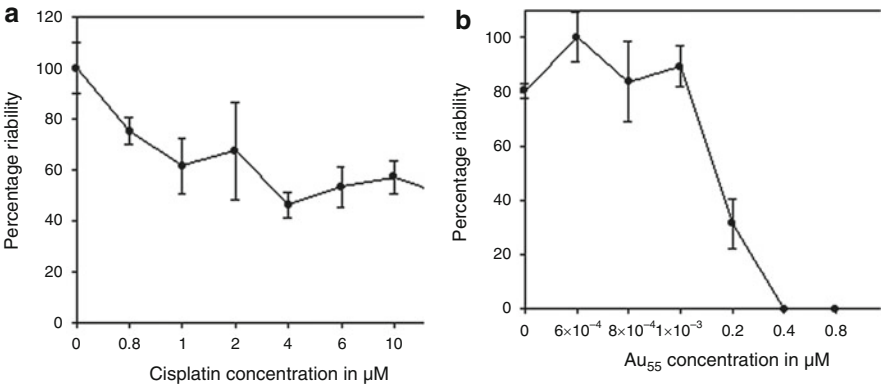

Fig. 13 Comparison of the viability of BLM cells treating them with cisplatin (**a**) and $Au_{55}(PPh_2C_6H_4SO_3Na)_{12}Cl_6$ (**b**). Figure reprinted with kind permission from [85]

used anticancer drug. Table 1 informs on the IC_{50} values of cisplatin and Au_{55}, i.e., the amount of material necessary to kill 50% of the cells. In each case, Au_{55} was more effective, especially considering the difference in time to reach IC_{50}, namely 24 h for Au_{55} and 72 h for cisplatin.

The difference between cisplatin and Au_{55} becomes also visible from Fig. 13a, b. BLM cells were treated with cisplatin and $Au_{55}(PPh_2C_6H_4SO_3Na)_{12}Cl_6$. Whereas the IC_{50} value for cisplatin is only reached with 50 μM, theAu_{55} cluster leads to the viability 0 with 0.4 μM [85].

In addition to the interaction with DNA, Au_{55} causes another reason for a fast cell death: oxidative stress. Necrosis and mitochondrial damage have been observed by incubation of HeLa cells, registered by flow cytometry [22, 86]. It is

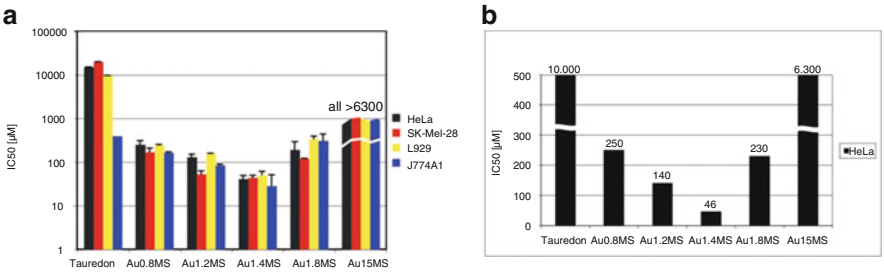

Fig. 14 (**a**) IC_{50} values (logarithmic scale) of four different types of cell lines in dependence of particle size. (**b**) Results for HeLa cells only in a linear scale (MS = monosulfonated triphenylphosphine, $PPh_2C_6H_4SO_3Na$). Figures reprinted with kind permission from [86]

known that larger AuNPs also cause oxidative stress. However, Au_{55} is, due to its structure and its special electronic properties, a much better source for oxidative stress. Its catalytic properties, based on the ability to excite O_2, but not to be oxidized itself (see Sect. 2, p. 9), contribute decisively to its toxicity. If the phosphine ligands are substituted by GSH, the toxicity is significantly reduced [22].

The question, if there is a size-dependent cytotoxicity of AuNPs, is still not answered by the experiments discussed above. A series of experiments with smaller and larger AuNPs, all equipped with $PPh_2C_6H_4SO_3Na$ molecules in the coating shell, give a clear answer. The cell lines HeLa, SK-Mel-28, L929, and J774A1 have been incubated with 0.8 (Au_9), 1.2, 1.4 (Au_{55}), 1.8, and 15 nm Au species [86]. Tauredon, a commercially available Au thiomalate complex, has been applied additionally. The result can be seen from Fig. 14.

As can be followed from Fig. 14a, b, the micromolar amounts for reaching the IC_{50} values for all four cell lines are a minimum for the 1.4 nm Au_{55} cluster. There is a lower toxicity for slightly smaller or larger particles, but without any doubt, Au_{55} is the most toxic one, as can better be seen from the linearly scaled Fig. 14b. The question, if such smaller or larger particles cause less toxicity for not ideally fitting into the major grooves or if reduced oxidative stress is responsible, cannot be answered yet. Some additional experiments concerning reactive oxygen species (ROS) shall be mentioned [22]. Oxidative stress in HeLa cells can be observed by using flow cytometry. However, 100 µM amounts of Au_{55} clusters cause heavy oxidative stress, increasing with increasing time (12–48 h). On the contrary, even 1,000 µM of 15 nm AuNPs do not cause any oxidative stress. As could be expected, 1.1 nm Au particles, coated with GSH, are also not able to generate oxidative stress, due to the much stronger bound thiol ligands that prevent formation of bare surfaces.

As already discussed, GSH-treated 1.4 nm Au_{55} clusters restored cell survival in contrast to the original phosphine-coated particles due to the existence of very strong Au–S bonds. Other sulfur-containing molecules such as *N*-acetylcysteine (NAC) on the cluster surface also reduce cytotoxicity. If the dissociation of TPPMS from the surface is hindered by excessive phosphine, cytotoxicity is also drastically

reduced, since the equilibrium of dissociation is shifted. However, GSH, NAC, and phosphines can also be considered as antioxidants. In order to exclude reducing properties of these compounds as reason for the restricted cytotoxicity, ascorbic acid as a strong reducer was tested. As could be expected, the cytotoxicity of $Au_{55}(Ph_2PC_6H_4SO_3Na)_{12}Cl_6$ was unchanged compared with experiments without ascorbic acid [22].These experiments clearly indicate the repeatedly mentioned condition that bare Au_{55} surfaces are necessary for the interaction with vital biological targets to observe cytotoxicity.

This finding is further corroborated by studies on the interaction of 1.4 nm Au clusters with ion channels [87]. The human ether-à-go-go-related potassium channel (hERG) is intensely studied and is known to interact with multiple molecular ligands. By patch clamp technique in hERG channel-transfected HEK293 cells, it was shown that 1.4 nm phosphine-stabilized AuNP irreversibly blocked hERG channels, whereas thiol-stabilized AuNP of similar size had no effect.

4 Properties In Vivo

4.1 Biodistribution

The toxicity phenomena discussed before have all been observed in cell cultures, i.e., in vitro. However, from experience we know that toxicity problems in a living being can be characteristically different depending on the kind of administration and distribution in the body. Radiolabeling by ^{198}Au isotopes allows very precise determination of the distribution in the different organs, though very low concentrations have to be used in order to avoid toxicity effects. In a series of experiments with 1.4, 5, 18, 80, and 200 nm AuNPs, all protected with the proven phosphine ligand $Ph_2PC_6H_4SO_3Na$, the influence of size on the biodistribution in healthy female Wistar–Kyoto rats in the course of 24 h has been studied [88–90]. γ-Spectroscopy has been applied to determine the gold content in the various organs. The administration was performed by intravenous injection (i.v., tail vein). As can be followed from Fig. 15, the 5, 18, 80, and 200 nm AuNPs are accumulated with 92–97% in the liver, in contrast to the 1.4 nm species which accumulates only with ca. 50% in this organ.

A detailed comparison of the biodistribution of 1.4 and 18 nm AuNPs is given in Fig. 16. A more or less quantitative accumulation of the 18 nm species in the liver can be registered, whereas 50% of the 1.4 nm clusters are distributed over the lung, spleen, kidney, blood, and urine [89, 90].

Considering the findings that traces of the 1.4 nm Au_{55} cluster could be found in the heart, brain, and uterus (not shown in Fig. 16), it clearly turns out that biodistribution of this species dominates, compared with larger AuNPs. Regarding its cell toxicity, Au_{55} particles must be considered as very dangerous if present in the blood stream.

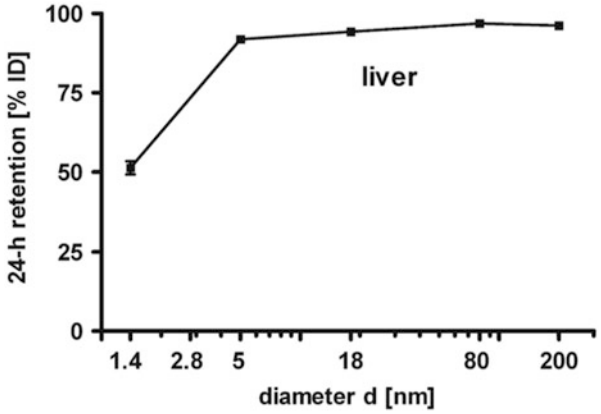

Fig. 15 Accumulation of 1.4, 5, 18, 80, and 200 nm AuNPs, all protected by $Ph_2PC_6H_4SO_3Na$, in the liver of rats after 24 h (i.v. injection). Figure reprinted with kind permission from [88]

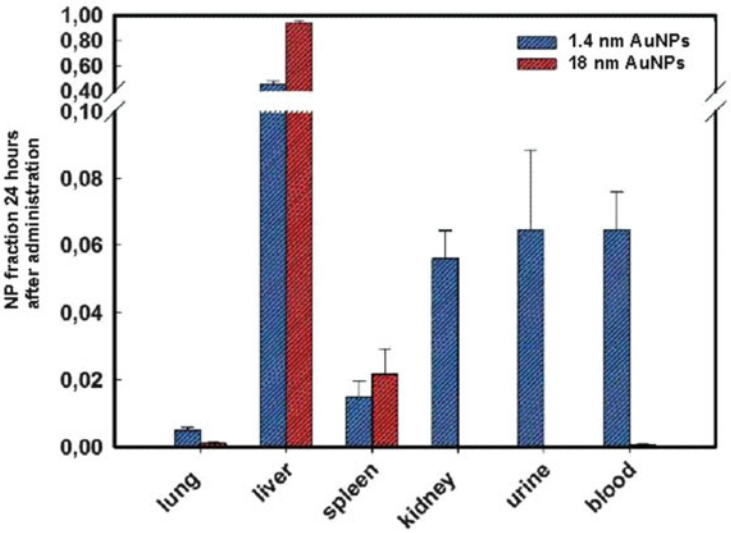

Fig. 16 Biodistribution of phosphine-coated 18 and 1.4 nm AuNPs after i.v. injection and 24 h retention. Figure adapted from [89]

There is still another question to be answered: which influence has the surface charge on biodistribution, if at all? Assuming a quantitative dissociation of the Na^+ ions, $Au_{55}(Ph_2PC_6H_{12}SO_3Na)_{12}Cl_6$ would be a 12-fold negatively charged particle; however, as we know, in a biological environment, substitution of the phosphines happens quickly. To study the influence of surface charge, strongly coordinated ligands have to be used, best guaranteed by Au–S bonds. Thioglycolic acid (TGA) is an ideal ligand system to investigate the influence of charge, because the carboxylic functions (COO^-) can be reacted with cysteamine (CA) in order to

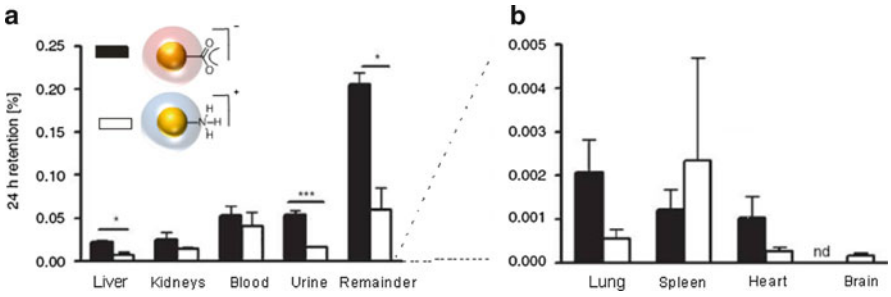

Fig. 17 Biodistribution of negatively and positively charged 2.8 nm AuNPs after intra-oesophageal application. Figure adapted from [91]

generate positive charges (NH_3^+). AuNPs (2.8 nm) coated with TGA and its positively charged derivative were used to find an answer [88]. As can already be followed from Fig. 15, phosphine-protected 2.8 nm particles accumulate less much in the liver compared with the larger particles by about 20%. The TGA-coated 2.8 nm particles accumulate with 81.6% in the liver, in good agreement with the also negatively charged phosphine-protected species. The positively charged CA-protected 2.8 nm particles assembled only with 72% in the liver with a higher concentration in other organs, for instance 11% in the spleen. As a conclusion it can be stated that biodistribution of positively charged AuNPs is slightly increased compared to negatively charged species.

An investigation, studying the absorption across intestinal barriers by intra-oesophageal instillation of phosphine-stabilized 1.4, 5, 18, 80, and 200 nm AuNPs as well as of TGA- and CA-covered 2.8 nm particles into healthy female rats showed again that biodistribution of the 1.4 nm clusters in secondary organs is maximum [91]. In contrast to the above-discussed situation, biodistribution of negatively charged TGA-coated 2.8 nm species was more expressed than that of the positively charged CA-protected particles of same size. Fig. 17 shows details.

4.2 Zebrafish: A New In Vivo Model

Due to the exponential growth of new nanomaterials and to the lack of screening assays and putative standards, there is a shortfall of correlative and predictive models to assess acute and chronic toxicities. This limits rapid preclinical development of new therapeutics and, therefore, it is of critical need to develop in vivo models which ideally maintain the biological representativeness. Small mammalian models are the most common method used to assess possible toxicities and biodistribution of nanomaterials in humans. Alternatively, *Danio rerio*, commonly known as zebrafish, has attracted much interest because of its unique features, manipulation accessibility, and short reproduction time [92–94]. Many fundamental

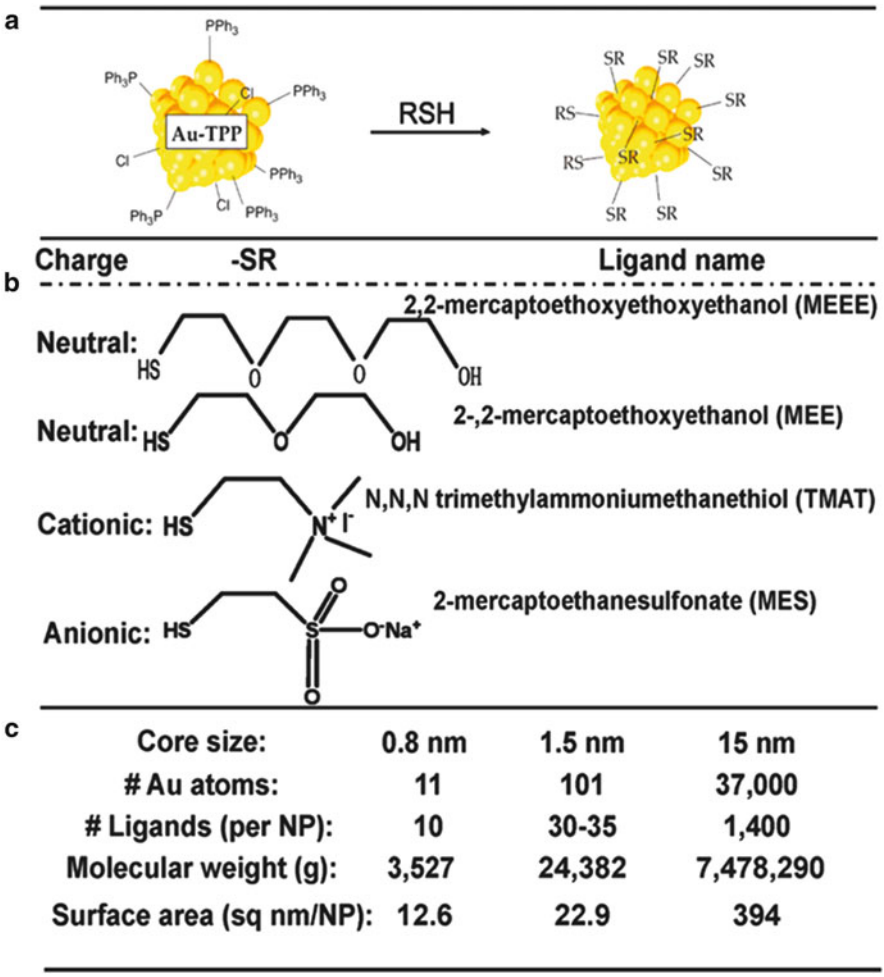

Fig. 18 (continued)

cellular and molecular pathways involved in the response to toxicants or stress are highly conserved between the zebrafish and mammals [95, 96].

Harper et al. tested AuNPs to determine the effect of core size, surface functionalization and charge on uptake rates, and the biological consequences of exposure [97]. AuNPs with core sizes of 0.8, 1.5, and 15 nm and positive, negative, and neutral surface charges were used (see Fig. 18). Chorions of fish embryos were chemically removed prior to the exposure of nanomaterials since the chorions may act as a physical barrier for AuNPs.

The 5-day exposure assay resulted in a clear surface charge-dependent toxicity. AuNPs with no charge do not adversely impact biological systems across a broad

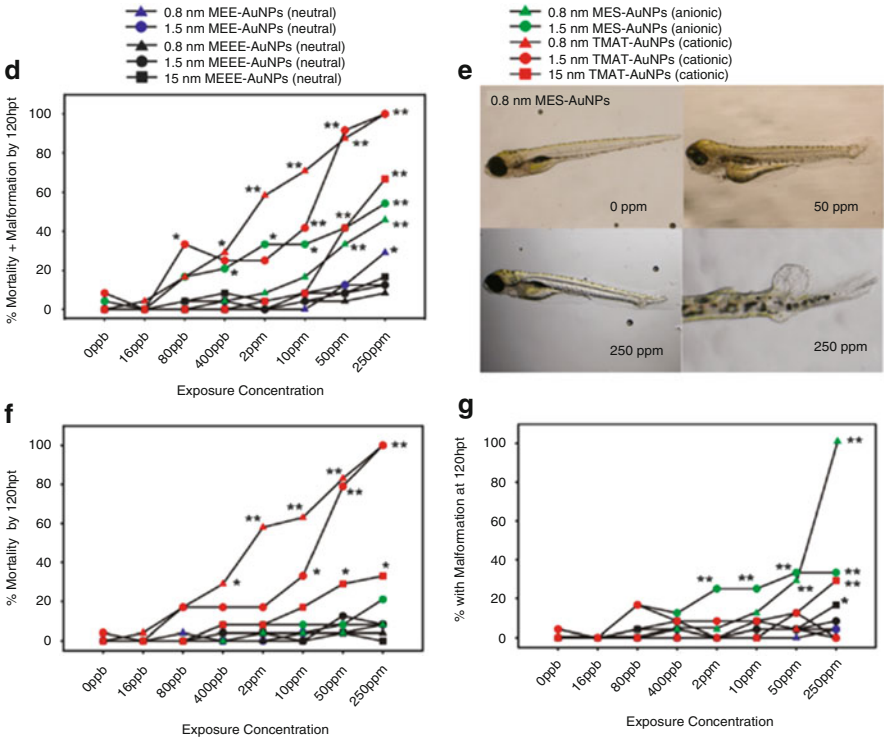

Fig. 18 AuNPs synthesis, structure, and properties. (**a**) Schematic scheme of the ligand exchange reaction starting from triphenylphosphine-stabilized AuNPs and leading to thiol-stabilized ones. (**b**) Charge, structure, and name for each ligand tested. (**c**) Chemical composition of the different AuNPs. Dose response results of embryonic zebrafish screen for tested AuNPs. (**d**) Percentage of zebrafish exhibiting either mortality or any malformation for each size and ligand tested across a spectrum of concentrations compared to control. (**e**) Examples of malformations seen upon exposure to 0.8 nm MES–AuNPs scored in the malformation category compared to control embryo. (**f**) Percentage of zebrafish dying after exposure to the AuNPs. (**g**) Percentage of zebrafish that survived but showing some malformation or abnormal behavior. Figure reprinted with kind permission from [97]

range of sizes. While positively charged TMAT–AuNPs primarily caused mortality, the negatively charged MES–AuNPs induced malformations (see Fig. 18). The uptake of the AuNPs was further investigated by instrumental neutron activation analysis (INAA), and it was shown that TMAT–AuNPs were not eliminated as rapidly as the other ones [97].

Pan et al. treated zebrafish embryos with TPPMS-capped 1.4 nm AuNPs (Au1.4MS), which were previously analyzed in HeLa cells [98]. In the cell test was shown that Au1.4MS was toxic while smaller and larger TPPMS-stabilized AuNPs were much less toxic [22, 86]. By the addition of GSH to Au1.4MS particles, the toxicity was inhibited due to replacement of the weak-binding TPPMS by the GSH hence resultant in a stronger gold thiolate bond [22].

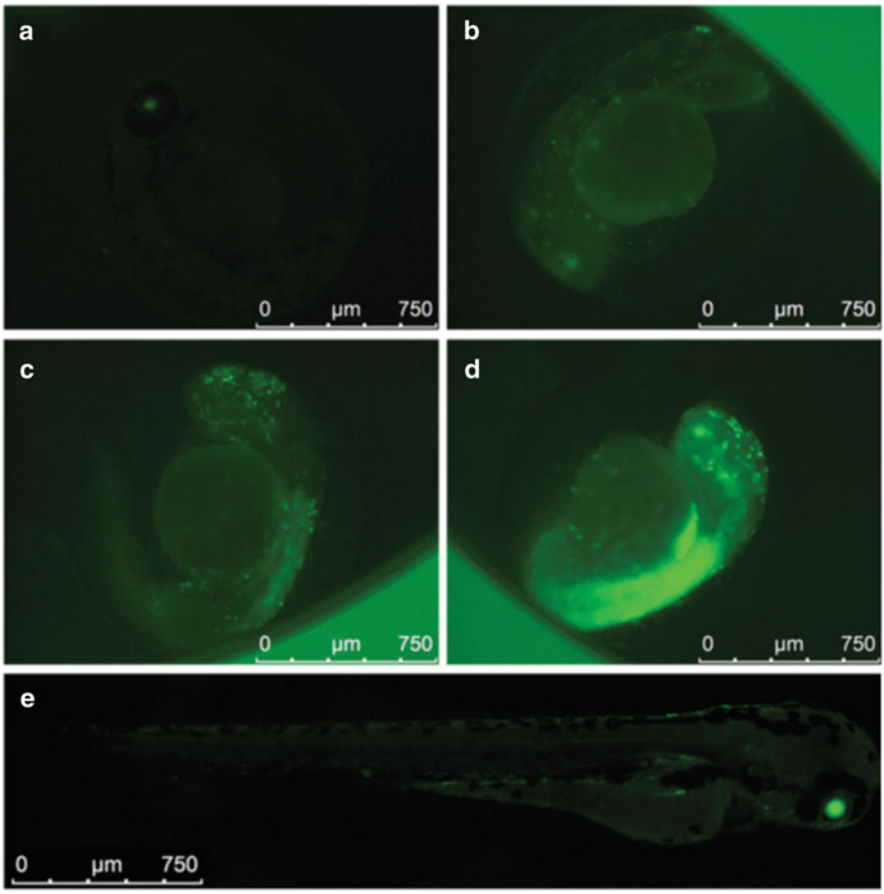

Fig. 19 Rapid induction of green fluorescent protein (GFP) expression in transgenic zebrafish triggered by toxic doses of Au1.4MS. Transgenic zebrafish embryos expressing GFP under the control of the heat shock protein were exposed to (**a**, **e**) embryo medium, (**b**, **d**) 200 µM Au1.4MS, and (**c**) 400 µM Au1.4MS. Spotty GFP signal was seen at 48 hpf in the presence of 200 µM Au1.4MS (**b**). The GFP signal increased with the toxic dose (**c**) and with time (**d**). In addition to the spotty GFP signal observed in the head region, strong GFP expression was present along the trunk at 48 hpf and was further enhanced at 72 hpf (**d**). Figure reprinted with kind permission from [98]

They showed that the toxicity in zebrafish model like in the cell culture depends on the size and ligand chemistry. At similar size AuNPs carrying ligands with high affinity to the gold atomic core were less toxic than AuNPs with more labile ligands. Along with the cytotoxicity of Au1.4MS-treated HeLa cells, the robust heat shock protein (HSP) stress response was observed. Therefore Pan et al. deemed transgenic heat shock reporter zebrafish ideal to test toxicity, teratogenicity, and upregulation of defense pathways. These transgenic zebrafish had similar responses to Au1.4MS-like wild-type zebrafish in terms of teratogenicity but were 20-fold more sensitive than wild type in reporting hepatotoxicity of Au1.4MS (Fig. 19).

Razansky et al. used PAI to image in vivo the expression of the fluorescence protein mCherry in the head of an adult transgenic zebrafish with a cross-sectional diameter of ~6 mm. The imaging results demonstrate the ability of the process to reveal many morphological features which matches well with the corresponding histology. Moreover, multispectral reconstructions accurately resolved fluorescence protein expression in the hindbrain of an intact living animal in high consistence with the corresponding epifluorescence image of the dissected brain [99].

5 Perspectives and Challenges

5.1 Cell Targeting

The examples given above illustrate some of the versatile applications of AuNPs in biological environments, addressing different fields in therapy and diagnosis and several recent reviews reflect that this is a rapidly evolving interdisciplinary research area [100]. However, any type of in vivo application should ideally follow the concepts of targeted delivery, which combines minimization of systemic exposure and, hence, decreased side effect with enhanced local concentration of the therapeutic or diagnostic agent for maximum efficacy. Cell targeting can be achieved along two conceptually different ways, i.e., passive and active targeting, respectively. While passive targeting utilizes, e.g., the enhanced permeability and retention (EPR) effect [101], by which small nanoparticles can accumulate in tumor tissue due to the disordered vasculature in tumors, active targeting relies on recognition molecules or molecular subunits, which can selectively bind to certain tumor cells and thus enhance the accumulation of the "targeting" compound at tumor sites. Although the passive targeting can lead to high uptake rates into the tumor tissue, the penetration into tumor interstitium is rather limited and varies the size or density of tumor tissue and is thus difficult to control. This may be enhanced by active targeting, as it was introduced for several types of "recognition molecules" bound to the surface of AuNPs, including small peptides [102, 103] and antibodies [104, 105]. One of the first promising examples was given in a study on targeted photothermal ablation of murine melanomas with targeted hollow gold nanospheres (HAuNs) of approx. 40 nm in diameter. It was found that the AuNPs were specifically taken up by melanoma cells associated with enhanced extravasation and dispersion into tumor matrix of targeted HAuNs compared to untargeted ones of the same size [105] (Fig. 20).

This control over biodistribution and localization of AuNPs gives rise to applications in nanomedicine, where AuNPs are utilized as efficient contrast agents for different imaging techniques, i.e., X-ray computed tomography (CT) and photoacoustic imaging (PAI). Furthermore therapeutic applications can be envisaged in the same manner, if an external stimulus such as light or X-ray

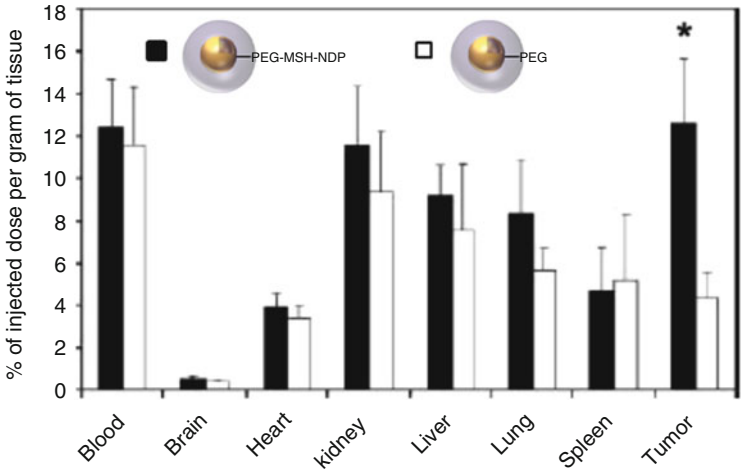

Fig. 20 Biodistribution of HAuNs targeted with NDP-MSH-PEG–HAuNs and untargeted, i.e., functionalized with PEG. Data are plotted as % of injected dose per gram of tissue. Mean FSD ($n = 5$). *, $P < 0.01$. Figure adapted from [105]

irradiation selectively addresses the AuNPs based on their size-dependent physical properties, such as SPR or X-ray radiosensitization. The potential applications that arise from these opportunities will be discussed in the following sections by means of selected examples.

5.2 *AuNPs as Contrast Agents in Molecular Imaging and as Therapeutic Agents*

Molecular imaging is an emerging field integrating molecular biology, chemistry, and radiology in order to gain understanding about biological processes and to identify diseases based on molecular markers, which appear earlier than the clinical symptoms [106]. The application of AuNPs in this area is increasing rapidly and offers excellent prospects for the development of new strategies for the diagnosis and treatment of cancer [107]. The reasons for this increasing attention to gold nanoconstructs are many: their size-dependent and shape-dependent plasmonic properties enable them to absorb and scatter light in the visible to NIR region, which may render them suitable for image-guided therapy and photothermal therapy (PTT). Significant synthetic advances now allow the design of AuNPs with highly controlled geometry, surface charge, physicochemical properties, and the decoration of their surfaces with polymers and bioactive molecules in order to improve biocompatibility and to achieve active targeting. This is stimulating the development of a diverse range of nanometer-sized objects that can recognize cancer tissue [107]. The use of the unique optical properties of AuNPs presents a

new opportunity for noninvasive imaging and therapy for a variety of diseases without exposing the rest of the body. Here, we introduce some imaging applications including X-ray computed tomography (CT) and photoacoustic imaging (PAI) and the opportunities of PTT as well as radiotherapy based on AuNP systems.

5.2.1 AuNPs for CT Imaging

X-ray computed tomography (CT) is clinically important because of its affordable price, high spatial resolution, unrestricted depth, and accurate anatomical information with reconstructed three-dimensional imaging [108]. The limitations of commercial iodine-based CT contrast agents such as rapid renal clearance, poor sensitivity, and toxicity have to be overcome, and AuNPs are interesting tools for that [109]. Their ability to absorb large amounts of X-ray radiation can be used to increase imaging contrast in diagnostic CT scans at lower radiation doses, which is based on the atomic weight of Au relative to atoms present in biological tissue. AuNPs have shown in vivo functionality as CT contrast agents for blood pool [110–116] and cancer imaging [117–124].

For passive targeting AuNPs are modified with PEG and its derivatives to enhance the circulation period in the blood. Kim et al. reinforced that by showing a 5.7 times higher attenuation of PEGylated AuNPs (~30 nm) than that of the current iodine-based CT contrast agent Ultravist [124]. Wang and his coworkers found that dendrimer-entrapped AuNPs can be detected through the attenuation of X-rays [117]. After either an intratumoral or an intraperitoneal administration of these particles, a xenograft tumor model could be imaged via CT.

The conjugation of antibodies or peptides onto the NP surface allows for active targeting. AuNPs with active tumor-targeting anti-HER2 antibodies enhance the visibility of millimeter-sized human breast tumors in mice in a 1.6-fold more efficient way than passive targeting AuNPs [123]. Chanda et al. reported enhanced CT attenuation of bombesin-functionalized AuNPs that selectively targeted cancer receptor sites that are overexpressed in the prostate, breast, and small-cell lung carcinoma [119]. Reuveni et al. demonstrated the in vivo feasibility of cancer diagnosis based on AuNPs as molecular markers using CT [118]. AuNPs with a diameter of 30 nm were functionalized with anti-epidermal growth factor receptor molecules and intravenously injected into nude mice implanted with human squamous cell carcinoma head and neck cancer. It is demonstrated that a small tumor, which is currently undetectable through anatomical CT, is enhanced and becomes clearly visible by the molecularly targeted AuNPs. As can be seen in Fig. 21, it is further shown that active tumor targeting is more efficient and specific than passive targeting with anti-rabbit IgG antibody-coated AuNPs with the same size.

Besides the imaging of cancer, Ghann et al. described a preparation of AuNPs with a core size of 10.7 nm that are stabilized with lisinopril via amine, disulfide, and thiol attachments to the AuNP surface to image the blood pool [115]. A stability study showed that the thiol lisinopril-coated AuNPs were the most stable ones and

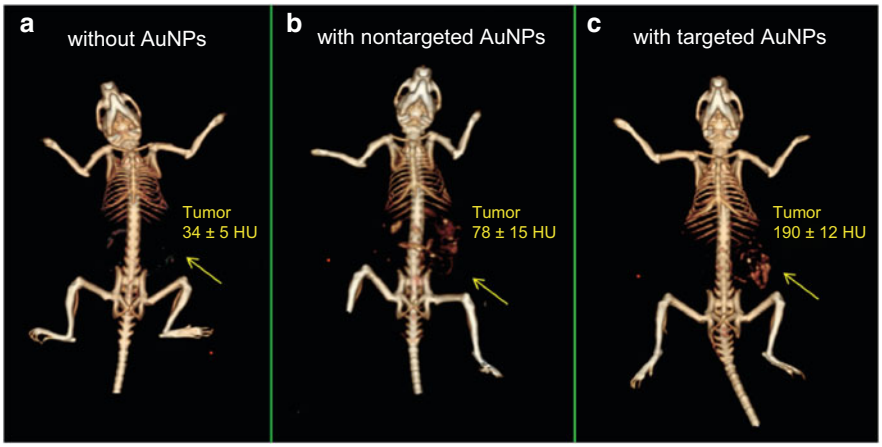

Fig. 21 In vivo X-ray CT volume-rendered images of mouse (**a**) before injection of AuNPs, (**b**) 6 h postinjection of nonspecific anti-rabbit IgG-coated AuNPs as a passive targeting experiment, and (**c**) 6 h postinjection of anti-epidermal growth factor receptor (EGFR)-coated AuNPs that specifically targeted the squamous cell carcinoma head and neck tumor. The anti-EGFR-targeted AuNPs show a clear contrast enhancement of the tumor (**c**, *yellow arrow*), which was undetectable without the AuNPs as contrast agents (**a**, *yellow arrow*). Figure adapted from [118]

therefore chosen for further studies to assess the targeting of angiotensin-converting enzyme (ACE) via X-ray CT. The resulting images displayed a high contrast in the region of the lungs and heart which indicates the targeting of ACE (see Fig. 22). The overexpression of ACE is associated with the development of cardiac and pulmonary fibrosis, and because of this the AuNPs could be a useful tool for the visualizing of cardiovascular pathophysiologies using CT imaging.

Cai and his coworkers injected PEG–GNPs with a size of 38 nm into adult mice via subcutaneous application [113]. Compared to the CT image contrast before PEG–GNP injection, the CT can produce clear images of the vascularity even 24 h after injection, indicating that the PEG–AuNPs have great potential as a blood-pool agent for CT imaging. In another study dendrimer-entrapped AuNPs with sizes in a range of 2–4 nm were injected subcutaneously into mice [110]. The vascular system could be imaged 5 and 20 min after injection and the urinary system could be imaged after 60 min. The feasibility for blood-pool CT imaging of PEGylated dendrimer-entrapped AuNPs after intravenous injection in rats and mice was explored as well resulting in an efficient blood-pool CT imaging of both rats and mice [116].

5.2.2 AuNPs for PAI Imaging

Photoacoustic imaging (PAI) is a technique which combines the advantages of optical and ultrasound imaging methods to visualize cancer tumor spreading and growth in vivo [125, 126] resulting in the ability to detect metal NPs with

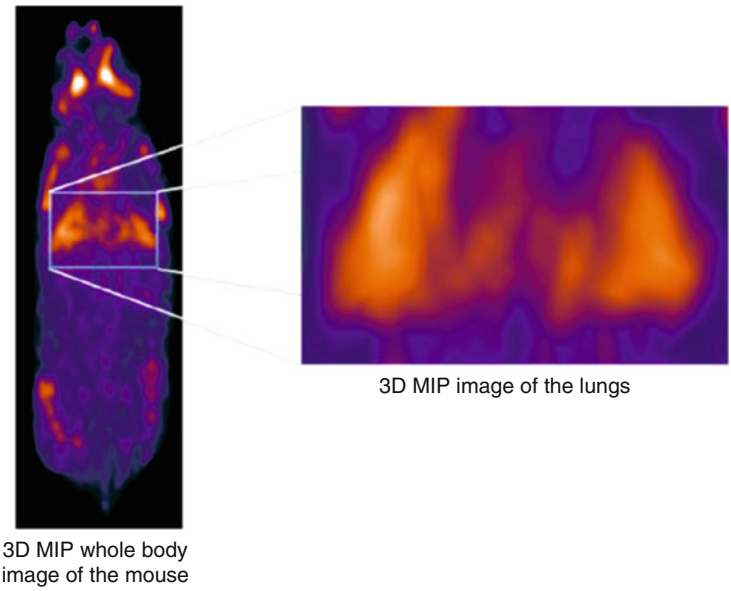

Fig. 22 3D subtraction CT image (measured at 80 and 140 kVp) of mice treated with thiol lisinopril-coated AuNPs resulting in a specific targeting of the lungs and heart (enlargement of the lungs and heart area on the right side). Figure reprinted with kind permission from [115]

nonionizing radiation relative deep in the tissue without the loss of high spatial resolution [126–128]. A temperature increase is induced by short pulses of electromagnetic irradiation in the range of strong absorbance. This causes a local increase in pressure via thermoelastic expansion leading to a generation of acoustic waves which can be detected with an ultrasound transducer [125–129].

AuNPs have gained immense interest for PAI since they combine size-dependent optical properties with a versatile surface chemistry [130–132]. As compared to the established group of organic dyes with its standard PAI contrast agent methylene blue (MB), recent research has demonstrated the superiority of AuNPs as they show high absorption cross sections combined with a resistance toward photobleaching. By controlling the particle size and geometry, the extinction characteristics of AuNPs can be tuned. Numerous groups have found that nanospheres [133–135], nanorods [136–143], nanoshells [132], hollow nanospheres [127], and nanocages [144–146] are eminently suitable.

The first studies with gold nanomaterials were done by Sokolov et al. who showed that 12 nm AuNPs conjugated with anti-epidermal growth factor receptor (anti-EGFR) antibodies specifically bound to EGFR proteins that are overexpressed on the surfaces of cervical cancer cells [147]. The receptor-mediated aggregation of AuNPs causes plasmon coupling of the clustered NPs, leading to an optical redshift of the plasmon resonances. Based on these results, the group of Emelianov demonstrated in ex vivo mouse tissue that multiwavelength photoacoustic imaging can detect cancer with high selectivity and sensitivity based on the plasmon

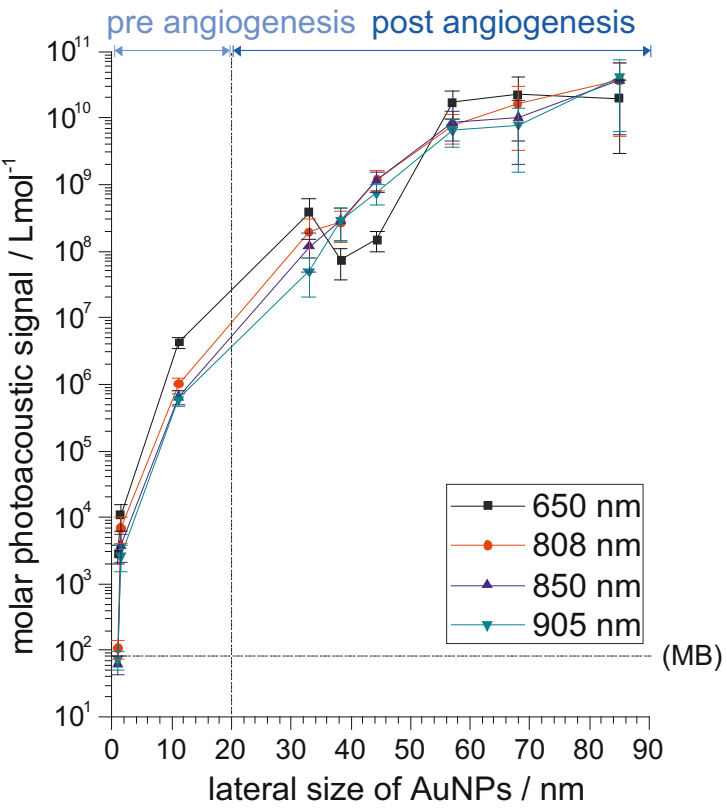

Fig. 23 Molar PA signal intensities as a function of the lateral particle size for the four laser excitation wavelengths. Error bars indicate the standard deviations evaluated with error propagation calculations resulting from statistical analysis of STEM micrographs. Lines are drawn to guide the eyes. Figure adapted from [150]

resonance coupling effect of the EGFR-targeted AuNPs [148, 149]. In addition to that plasmon resonance coupling AuNPs have been suggested for imaging of macrophages in atherosclerotic plaques for an early detection of cancer [133].

In a recent study, Gutrath et al. showed that the molar extinction of spherical AuNPs with core diameters of 1.0, 1.4, and 11.2 nm, gold nanorods (AuNRs) with longitudinal/transversal elongation of 38/9 and 44/12 nm, and HAuNs' with outer/inner diameters of 33/19, 57/30, 68/45, and 85/56 nm can be correlated with the molar PA signal intensity of the respective AuNPs [150]. For increasing lateral particle size, increasing molar photoacoustic signal intensity is observed, which is shown in Fig. 23. The studied AuNPs exhibit significantly larger molar PA intensities as compared to the commonly used dye MB, except for spherical Au1.0NPs, which exhibited results comparable to the values of MB. The particle-size-dependent evaluation of the PA signal intensities is of great interest because larger particles are useful to obtain molecular imaging of post-angiogenesis

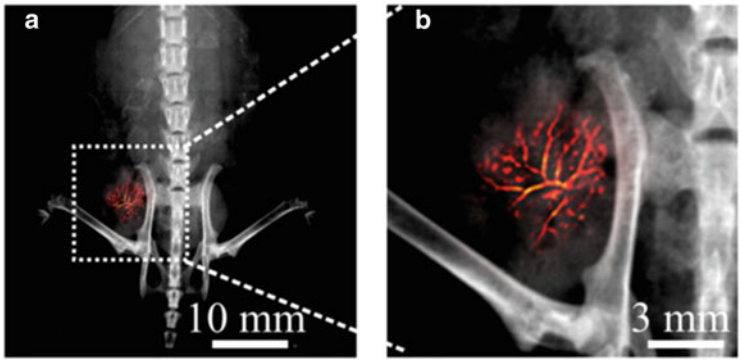

Fig. 24 Combined X-ray and PA images of a mouse tumor in vivo, which clearly show the location and the blood vessels of the tumor. (**a**) Overlay of X-ray image and PA image. (**b**) Enlargement of the corresponding image area highlighted by an inset in panel **a**. Figure reprinted with kind permission from [156]

processes, whereas only small NPs are able to infiltrate the nonvasculated parts of tumors for efficient targeting. These results were confirmed by Popović et al. who observed that particles within the 10–150 nm-size range show a particle-size-dependent uptake mechanism after injection into a mouse bearing a Mu89 human melanoma xenograft [151]. When a mixture of 12, 60, and 125 nm particles is injected in vivo the 12 nm particles extravasated easily and diffused from the vessels with minimal hindrance, the 60 nm particles extravasated but do not leave the immediate perivascular space, while the 125 nm particles did not appreciably extravasate.

By using anti-HER2-conjugated AuNRs, Agarwal et al. detected prostate cancer with PAI [139]. This method can also be used to detect and localize AuNRs with an approximate size of 50 × 15 nm at a very low concentration deep within tissue [152]. AuNRs of varying aspect ratios (3.7 and 5.9) and functionalized with different molecules to target MBT2 and HepG2 cells were used by Li et al. [153]. Jokerst et al. varied the aspect ratios of AuNRs in the range of 2.4–3.5, and those with an aspect ratio of 3.5 showed the highest ex vivo and in vivo PA signal [154]. Therefore these particles were used to image subcutaneous xenografts of the 2008, HEY and SKOV3 ovarian cancer cell lines in living mice. A linear relationship between the PA signal and the concentration of the injected AuNRs was observed. Another study demonstrated multiple selective targeting on oral cancer cells with HER2-antibody-(aspect ratio of 3.7) and EGFR-antibody-conjugated AuNRs (aspect ratio of 5.9) [155]. Huang et al. demonstrated a combined cancer imaging method using X-ray and PAI with PEG–AuNRs as contrast agents [156]. Figure 24 shows that the combination of X-ray and PAI can provide more comprehensive details of the tumor such as position, size, and vascular network. This is of great interest because vasculature regulates the metabolic and hemodynamic states of biological tissues wherefore the visualizing of blood vessels enables the tracking of cancer metastasis and monitoring of tumor angiogenesis.

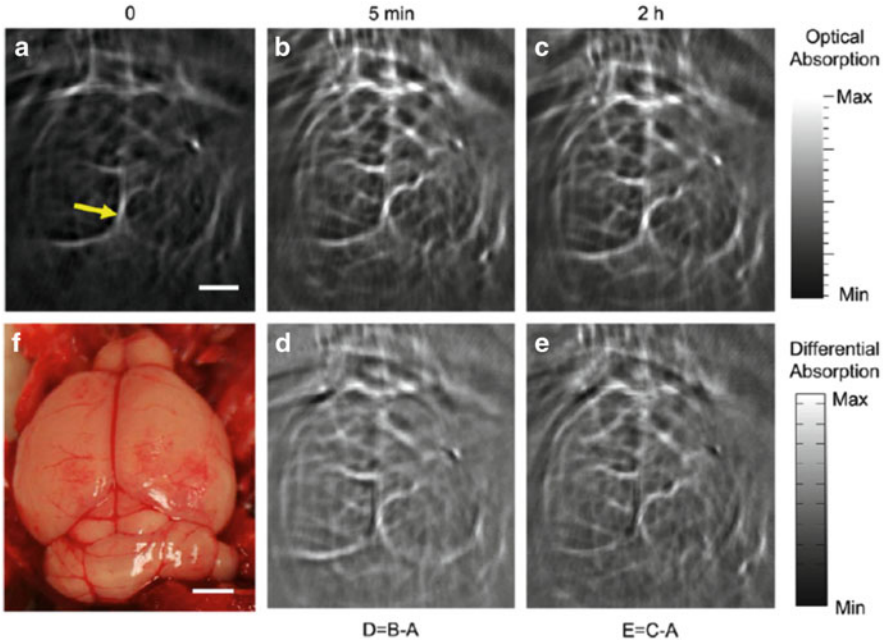

Fig. 25 Noninvasive PA images of a mouse brain in vivo employing PEG–HAuNs and NIR light at a wavelength of 800 nm. PA images received (**a**) before (the arrow pointed on the middle cerebral artery), (**b**) 5 min after, and (**c**) 2 h after the intravenous injection of PEG–HAuNs. (**d**, **e**) Differential images obtained by subtracting the preinjection image from the postinjection images (Image **d** = Image **b** − Image **a**; Image **e** = Image **c** − Image **a**). (**f**) Open-skull photograph of the mouse brain cortex obtained after the data acquisition for PAT. Scale bar = 2 mm. Figure reprinted with kind permission from [127]

The application of PEGylated hollow gold nanospheres (HAuNs) with a diameter of ~40 nm in nude mice showed the brain vasculature with great clarity and more detail structures. The images shown in Fig. 25 depicted blood vessels as small as ~100 mm in diameter which could be clearly seen with PEG–HAuNs as PAI system [127].

Beneath AuNPs, AuNRs, and HAuNs, also gold nanocages (AuNCs) have shown great promise in PAI. In one report, 50 nm AuNCs were intradermally injected on the left forepaw pads of Sprague–Dawley rats to image sentinel lymph nodes (SLN) noninvasively [157]. With the passing of time, the contrast at the SLN gradually and the PA signal within the SLN were increased. It was also demonstrated that the total image depth below the skin surface of 33 mm could be reached with good contrast which is substantial because this depth is greater than the mean depth of SLNs in human beings [157]. PEGylated AuNCs were used by Yang et al. to confirm the contrast enhancement for PA imaging in vivo [146]. The particles were injected into Sprague–Dawley rats via the tail vein and better resolved images of the cerebral cortex after administration were recorded. For the

visualizing of this layer in the brain of Sprague–Dawley rats, also PEGylated gold nanoshells were used by injection via the tail vein as well [132]. The nanoshells were administrated three times successively, and after the final injection the rat brain was imaged sequentially 10 times for more than about 6 h. The PA signal enhancement after the injection as a function of time was quantified with a maximal signal increase of about 63%.

In a recent report Bao et al. used PEGylated gold nanoprisms (AuNRs) with a uniform thickness of ca. 10 nm, with three congruent edge lengths of ca. 120 nm in in vivo settings [158]. The mice were treated with this AuNRs in order to visualize tumor angiogenesis in gastrointestinal cancer cells. It is shown that the AuNRs have the capacity to penetrate tumors and provide a high-resolution signal amplifier for PAI.

5.2.3 AuNPs as Agents for Photothermal Therapy

As compared to the diagnostic approach followed by PAI during photothermal experiments, a therapy approach is proposed by photothermia. Due to their SPR properties AuNPs are able to absorb light from incident radiation with high efficiency (extinction coefficient ~10^9 M^{-1} cm^{-1}) [159] in the near-infrared (NIR) region of the electromagnetic spectrum and convert it into heat [83, 160, 161]. The generated heat is subsequently delivered to the immediate surroundings of the AuNPs and allows a highly specific thermal ablation of diseased or infected tissue [162–165]. The advantage of the use of light in the NIR region is that the tissue damage and attenuation by biological fluids and tissues are minimal.

In 2003 Pitsillides et al. were the first who demonstrated that AuNPs can be used for PTT [166]. Since that time, several other studies have examined the use of AuNPs in PTT. Nam and coworkers designed AuNPs with a size of 10 nm with a pH-dependent agglomeration behavior [167]. The incubation of HeLa and B16 F10 mouse melanoma cells with these AuNPs shows an aggregation of the AuNPs in a typical tumor intercellular pH, leading to a shift of their absorption to the far- and near-IR spectral regions and thus to a utilization in PTT.

Nevertheless, AuNRs [168], HAuNs [105], AuNCs [104, 144, 169–171], and gold/silica nanoshells [172] with SPR frequencies in the NIR range are more promising agents for PTT because the absorption of the NPs can be tuned by synthetically varying the aspect ratio and shell thickness : core radius. The latter were some of the first applied in PTT by Halas and West [172–175]. Based on efficiently destroying breast carcinoma cells with PEGylated silica/gold nanoshells, the particles were injected into the tumor interstitium of SCID mice bearing sarcoma xenografts. A subsequent NIR light exposure demonstrated a 4–6 mm depth of thermal damage [172]. Later on NIR PTT was demonstrated using systemically administered PEGylated nanoshells in a colon cancer mouse model. All tumors in nanoshell-treated mice were completely ablated after a single PTT treatment and the animals appeared healthy and tumor free for more than 90 days posttreatment. In contrast the tumors of the control animals and the additional

sham-treated animals (laser treatment without nanoshell injection) continued to grow, with nearly 50% mortality at day 10 [174].

For vascular-targeted PTT of glioma nanoshells were conjugated to VEGF and/or PEG to thermally ablate VEGF receptor-2-positive endothelial cells upon NIR laser irradiation [176]. It was observed that VEGF-coated but not PEG-coated nanoshells bound to VEGF receptor-2-positive cells in vitro to enable targeted photothermal ablation. Subsequent in vivo studies in mice-bearing intracerebralglioma tumors showed that VEGF targeting could double the proportion of nanoshells bound to tumor vessels and vasculature was disrupted following laser exposure.

AuNPs with an interior composition of gold sulfide, or gold/gold sulfide composite structures, were first produced by self-assembly by Zhou et al. and were shown to have strong NIR-absorbing properties [177]. Gobin et al. compared gold/gold sulfide AuNPs with an overall diameter of 35–55 nm that provides higher absorption as well as potentially better tumor penetration, with gold/silica nanoshells with an overall diameter of 120–160 nm [178]. At relatively low concentrations and laser powers, the heating profiles of gold/gold sulfide AuNPs showed temperatures high enough to effect tumor ablation by hyperthermia. The smaller size of the gold/gold sulfide NPs yields a particle with higher absorbing cross-sectional area ratio than the gold/silica nanoshell.

Hu et al. noted that AuNRs and AuNCs have much larger absorption and scattering cross sections than nanoshells wherefore these are better candidates for PTT [179]. The use of AuNRs, which can more efficiently absorb photons to generate heat, as PTT agent is based on the pioneering work of Catherine Murphy's group [180]. These particles have been extensively studied for PTT applications in vitro [168, 181, 182] and in vivo [183, 184]. Fundamental work by El-Sayed and coworkers has provided insights into how to optimize metallic NP-based PTT, including how shape influences heat generation efficiency [185] and the critical temperatures associated with therapy (typically 70–80°C) [186]. They also found that AuNRs labeled with an EGFR-targeting ligand were effective for PTT under NIR illumination in vitro [168]. The feasibility of in vivo PTT treatment of squamous cell carcinoma xenografts with PEGylated AuNRs was demonstrated by the inhibition of average tumor growth for direct and intravenous delivery methods [183].

Von Maltzahn et al. described an approach to improve plasmonic therapy by using computational simulations to understand the effect of NP concentration on heating in vivo. Therefore an X-ray CT scan was utilized to characterize the distribution of intratumorally and intravenously administered PEGylated AuNRs in human tumor xenograft bearing mice. The high absorption efficiency of the AuNRs in both the X-ray and NIR regions enabled real-time visualization and therapy [187]. To assess the utility of the high X-ray absorption of PEG–NRs for detection of in vivo, PEG–AuNRs were directly injected into the tumors of mice bearing bilateral human MDA-MB-435 tumors, implanted either in the mammary fat pad or the rear flank. It was found that X-ray CT rapidly detailed

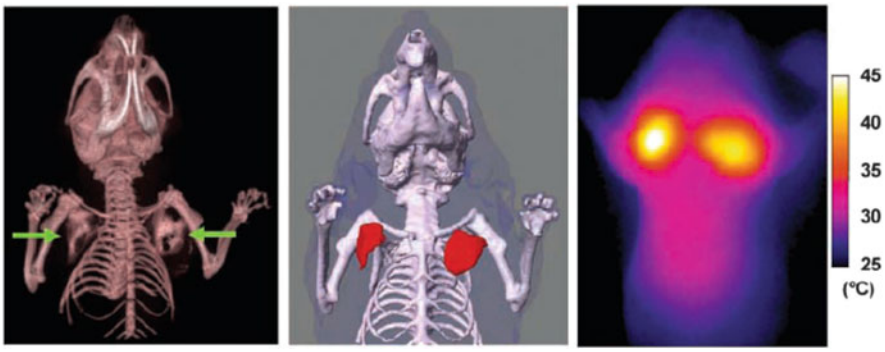

Fig. 26 Photothermal heating of passively targeted AuNRs in tumors. PEG–AuNRs or saline was given i.v. to mice bearing MDA-MB-435 tumors on opposing flanks. After AuNRs had cleared from circulation (72 h after injection), the right flank was irradiated (beam size indicated by *dotted circle*). Figure reprinted with kind permission from [187]

the three-dimensional distribution of PEG–NRs in tumors, showing clear distinction between AuNRs and soft tissues, as seen in Fig. 26.

To prolong the circulation time, optimize the tumor targeting, and decrease the liver uptake, Choi et al. prepared AuNR-loaded, chitosan-conjugated, pluronic-based nanocarriers which could serve as imaging agents for cancer cells and as a very effective hyperthermia agent for PTT [184]. By delivering the nanocarriers via an intravenous injection followed by NIR laser irradiation to the tumor site resulted in a very efficient thermolysis in vivo, achieving a complete tumor resorption without damage to the surrounding tissue.

Xia and coworkers studied AuNCs as photothermal transducers for therapeutic applications [104, 144, 169–171]. They utilized PEGylated AuNCs with an edge length of 45 nm for selective destruction of neoplastic tissue using a bilateral tumor model. The particles accumulated in tumors with a relatively high efficiency leading to a slightly higher amount of AuNCs in the tumor periphery than in the inner core. With an infrared camera the temperature increase during photothermal treatment was monitored which is shown in Fig. 27.

The effect of PTT on cells by larger, more rapid temperature increases, often referred to as “ablative” treatments, is considered to be necrosis with the corresponding melting of cell membranes and organelles [188]. In contrast to that mild temperature increases (known as hyperthermia), mostly proceed via apoptotic pathways, and are known to perturb a variety of normal cellular functions [183]. Huang et al. designed AuNR elastin-like polypeptide matrices loaded with the heat shock protein (HSP) inhibitor 17-(allylamino)-17-demethoxygeldanamycin (17-AAG) to give insights into the release of heat shock proteins (HSPs), which help to restore normal processes to the cell, and their relation to PTT [181]. They demonstrated that AuNRs in combination with 17-AAG improve significantly (>90%) death of cancer cells, while “single treatments” (i.e., hyperthermia alone and 17-AAG alone) demonstrated minimal loss of cancer cell

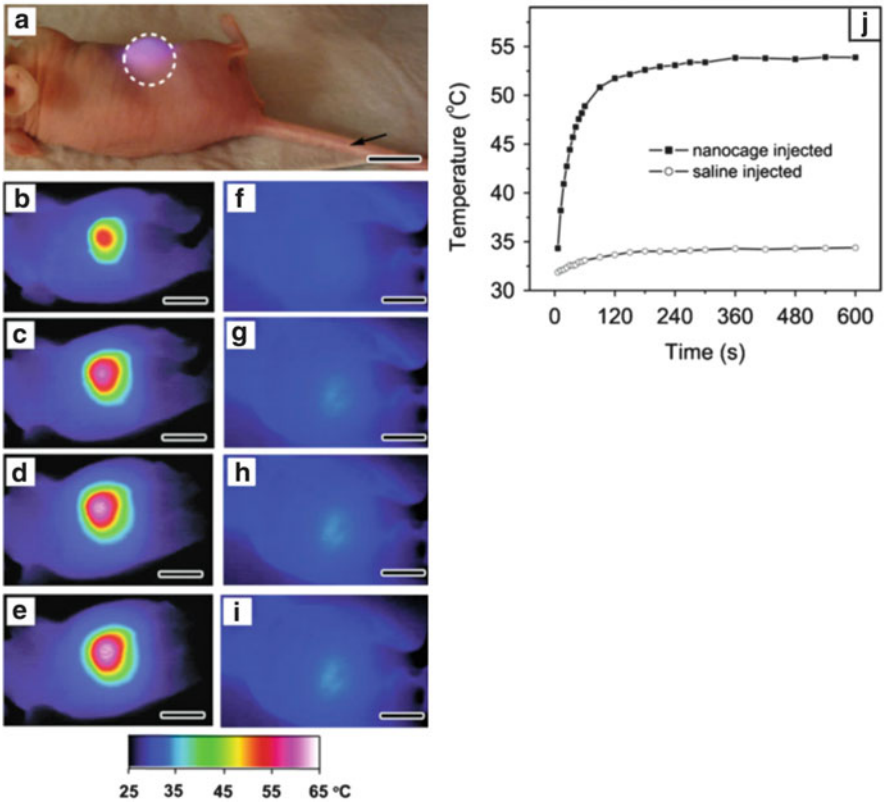

Fig. 27 (**a**) Photograph of a tumor-bearing mouse under photothermal treatment. PEGylated nanocages or saline was administrated intravenously through the tail vein as indicated by an *arrow*. After the NCs had been cleared from the circulation (72 h after injection), the tumor on the right flank was irradiated with a beam size indicated by the dashed circle. (**b**–**g**) Thermographic images of nanocage-injected (**b**–**e**) and saline-injected (**f**–**i**) tumor-bearing mice at different time points: (**b**, **e**) 1 min, (**c**, **f**) 3 min, (**d**, **g**) 5 min, and (**e**, **i**) 10 min. (**j**) Plots of average temperature within the tumors (*dashed circle*) as a function of irradiation time. All scale bars are 1 cm. Figure reprinted with kind permission from [170]

viability (<10%). This result seems to imply that in addition to the local thermal effects, significant improvements in NP-mediated PTT can also take advantage of limiting cellular responses.

5.2.4 AuNPs in Radiotherapy

Another method which is widely used to help reduce tumor size is through radiofrequency. Since the early 1990s, it has been utilized as a treatment for destroying liver tumors [189]. However, this method does have its drawbacks,

such as accuracy, invasive needle placement, and toxic effects, on the tissue surrounding the tumor and also on internal organs [190, 191]. These side effects have a drastic limitation on the amount of radiation used during treatment.

Several studies have focused on the use of AuNPs as novel high-Z radiosensitizing agent to increase the sensitivity of tumors irradiated with clinical X-ray beams [192, 193]. Numerous experimental [194–196] and theoretical studies [197–199] have shown that clinically significant enhancements are achievable with AuNPs-treated tumors in combination with X-ray therapy.

In vitro studies showed AuNP radiosensitization by irradiation of cells and plasmid DNA [200–204]. Irradiating plasmid DNA in the presence of 5 nm AuNPs leads to single-strand and double-strand break enhancement [202]. Rahman et al. observed a biological dose enhancement factor of up to 24.6 when irradiating bovine aortic endothelial cells in the presence of 1.9 nm AuNPs [203]. Roa et al. were the first who reported that 10.8 nm glucose-capped AuNPs trigger the activation of CDK kinases leading to cell cycle accumulation in the G2/M phase and acceleration in the G0/G1 phase [205]. This leads to the suggestion that p53 and the CDK kinases are targets for AuNPs. A striking sensitization to ionizing radiation is achieved as well. In another study AuNPs with an approximate size of 45 nm showed an increase of the effectiveness of proton radiotherapy for the killing of prostate tumor cells of about 15–20% [206].

Despite the rapid increase of in vivo studies investigating the uptake and distribution of AuNPs, there remains a lack of studies of in vivo radiosensitization with these particles. In 2004, the suitability of AuNPs for radiotherapy was examined by Hainfeld et al. in vivo [192]. Nontargeted 1.9 nm AuNPs (AuroVist) in combination with 250 kV radiation were shown to prolong survival in Balb/C mice bearing EMT-6 murine breast cancer tumors. One month after the treatment, a dramatic reduction in tumor growth was observed. Based on these results, a second experiment with a longer follow-up study in mice which received a slightly lower radiation dose alone or with AuNPs was pursued. A remarkable tumor regression in mammary tumors and long-term survival without any significant toxicity were demonstrated thus indicating the utility of these particles for radiotherapy. In a recent study by Hainfeld et al., a highly radioresistant murine squamous cell carcinoma was used in mice [207]. A significant tumor growth delay and a long-term tumor control were observed by combining AuNPs with irradiation. Chang et al. used 13 nm citrate-stabilized AuNPs in a mouse model with B16F10 murine melanoma cells. A significant in vivo tumor growth delay and increased survival were noted when AuNPs were injected 24 h before irradiation [195]. The median survival of the mice with 65 days was shorter than in the Hainfeld study but the AuNP concentration used is much lower.

While demonstrating the potential efficacy of AuNP radiosensitization, the large variations in these studies revealed AuNP radiosensitization to be highly sensitive to a number of physics and pharmacological parameters such as irradiation energy, AuNP size and concentration, and intracellular localization [192, 202, 203]. Toward understanding and predicting the effects of these parameters, there have been a number of Monte Carlo simulation studies exploring AuNP dose enhancement [197, 198, 208–213].

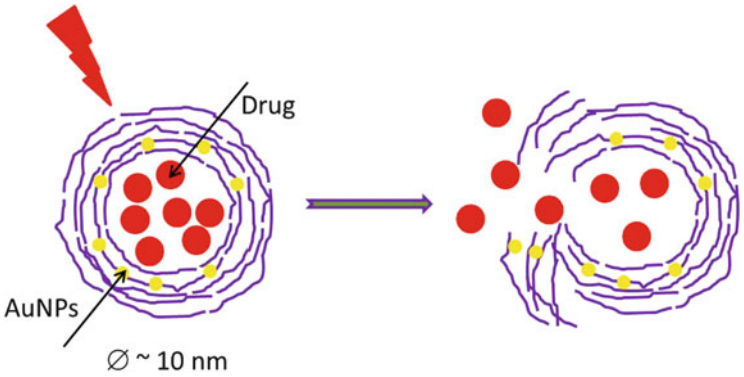

Fig. 28 Sketch of the opening process of a polymer container filled with the drug and additionally containing AuNPs for photoinduced heating process. Figure adapted from [90]

5.3 Drug Delivery

If AuNPs shall be used as therapeutic agents based on their cytotoxicity in the future, a fundamental challenge has to be faced. One of the most common drawbacks of the present treatment of tumors is the small specificity of the respective drugs that means that the number of damaged tumor cells compared with the number of damaged healthy cells is far too small. Therefore, worldwide efforts are being made to improve the situation, among others by using the so-called drug delivery (drug release) systems. The goal is to transport a drug specifically into a tumor in order to avoid damage of healthy cells as far as possible. One promising attempt is the use of micro- or nano-sized hollow containers which are filled with chemotherapeutics or cytotoxins. The advantage of this technique is the possibility to modify the surface of the capsules by tumor-specific antibodies without the need to modify the drug itself. Accumulated in the tumor, the containers open themselves or by stimuli from outside, for instance, by photoinduced heating of AuNPs, also present in the containers [163, 166, 214–216]. The capsules usually consist of polymers which can easily be modified by tumor-specific antibodies. Poly (alkylcyanoacrylate) even degrades rapidly in vivo without any photoinduction of AuNPs [217]. Figure 28 elucidates the artificial opening process using AuNPs.

The use of AuNPs for photoinduced heating is only of importance for the opening of the polymer containers. Another chance is the direct use of AuNPs as a drug. The cell toxicity of Au_{55} with its ultrasmall 1.4 nm diameter has already been discussed in Sect. 3. Experiments to transport 1.4 nm Au particles in polymer spheres are presently under investigation (Simon U, Mayer C, private communication).

Though not yet tested for the use of AuNPs, mesoporous silica nanoparticles are a promising alternative to hollow nanospheres. They are intensively under investigation, especially to study single particle tracking to living cells by fluorescence microscopy allowing the discrimination between active transport and random motion [218–220].

Also still under investigation for use as drug delivery systems are the so-called polymersomes. Polymersomes consist of a double layer of polymers with a hydrophilic and a hydrophobic function, cross-linked by various polymers. The combinations form a hollow sphere, comparable with the structure of liposomes from which the name polymersome derives. Their size can be varied between 100 nm and 100 μm [221]. They are able to transport bioactive molecules to the relevant cells and to release them there [222].

6 Summary

This review has summarized relevant aspects on the properties and the bioresponse of AuNPs in the context of a rapidly growing field of applications, i.e., the application in vivo and in vitro for medical purposes. It has been shown by a number of selected examples that most of the AuNPs synthesized so far are considered nontoxic, making them suited for in vivo applications, e.g., for imaging and therapy. Special focus is laid on AuNPs in the sub-2 nm range, which under certain conditions can become toxic. This sheds light on how adverse effects of AuNPs in biological systems may occur and, at the same time, suggests how such toxic effect may be used in therapy as well. The present state of knowledge is summarized on the mechanism how such small AuNPs may interact with biomolecules and cells, addressing the effect of shape complementarity in the sense that AuNPs approach the size of biological molecules and subcellular structures and thus may even behave as molecular ligands.

It becomes evident that the high degree of control over particle size and ligand chemistry opens up an avenue of novel applications in a biological environment.

References

1. Teo BK, Shi X, Zhang H (1992) Pure gold cluster of 1:9:9:1:9:9:1 layered structure: a novel 39-metal-atom cluster $[(Ph_3P)_{14}Au_{39}Cl_6]Cl_2$ with an interstitial gold atom in a hexagonal antiprismatic cage. J Am Chem Soc 114:2743
2. Gutrath BS, Oppel IM, Presly O, Beljakov I, Meded V, Wenzel W, Simon U (2013) $[Au_{14}(PPh_3)_8(NO_3)_4]$: an example of a new class of $Au(NO_3)$-ligated superatom complexes. Angew Chem Int Ed 52:3529
3. Briant CE, Theobald BRC, White JW, Bell LK, Mingos DMP, Welch AJ (1981) Synthesis and X-ray structural characterization of the centred icosahedral gold cluster compound $[Au_{13}(PMe_2Ph)_{10}Cl_2](PF_6)_3$; the realization of a theoretical prediction. J Chem Soc Chem Commun 201
4. Mingos DMP (1976) Molecular-orbital calculations on cluster compounds of gold. J Chem Soc Dalton Trans 1163
5. Mingos DMP (1996) Gold – a flexible friend in cluster chemistry. J Chem Soc Dalton Trans 561

6. Gutrath BS, Englert U, Wang Y, Simon U (2013) A missing link in undecagold cluster chemistry: single-crystal X-ray analysis of $[Au_{11}(PPh_3)_7Cl_3]$. Eur J Inorg Chem 2013 (12):2002–2006
7. Schwerdtfeger P (ed) (2002) Relativistic electronic structure theory, part 1: fundamentals. Elsevier, Amsterdam
8. Schwerdtfeger P (ed) (2005) Relativistic electronic structure theory, part 2: applications. Elsevier, Amsterdam
9. Hess BA (ed) (2002) Relativistic effects in heavy-element chemistry and physics. Wiley-VCH, New York
10. Mie G (1908) Beiträge zur Optik trüber Medien, speziell kolloidaler Metallösungen. Ann Phys 330:377
11. Schmid G, Brune H, Ernst H, Grunwald A, Grünwald W, Hofmann H, Krug H, Janich P, Mayor M, Rathgeber W, Simon U, Vogel V, Wyrwa D (2006) Nanotechnology: assessment and perspectives. In: Wissenschaftsethik und Technikfolgenabschätzung, vol. 27. Springer, Berlin
12. The Royal Society and The Royal Academy of Engineering, Science Policy Section (2004) Nanoscience and nanotechnologies: opportunities and uncertainties. The Royal Society and The Royal Academy of Engineering, Science Policy Section, London
13. Bezryadin A, Dekker C, Schmid G (1997) Electrostatic trapping of single conducting nanoparticles between nanoelectrodes. Appl Phys Lett 71:1273
14. Schmid G, Pfeil R, Boese R, Bandermann F, Meyer S, Calis GHM, van der Velden JWA (1981) $Au_{55}[P(C_6H_5)_3]_{12}CI_6$ — ein Goldcluster ungewöhnlicher Größe. Chem Ber 114:3634
15. Chi LF, Hartig M, Drechsler T, Schwaack T, Seidel C, Fuchs H, Schmid G (1998) Single-electron tunneling in Au_{55} cluster monolayers. Appl Phys A 66:187
16. van der Velden JWA, Vollenbroek FA, Bour JJ, Beurskens PI, Smits JMM, Bosman WP (1981) Recueil J Roy Netherlands Chem Soc 100:148
17. Schmid G, Morun B, Malm J-O (1989) $Pt_{309}Phen^*_{36}O_{30 \pm 10}$, a four-shell platinum cluster. Angew Chem Int Ed 28:778
18. Schmid G, Klein N, Morun B, Lehnert A (1990) Two, four, five-shell clusters and colloids. Pure Appl Chem 62:1175
19. Boyen HG, Ethirajan A, Kästle G, Weigl F, Ziemann P, Schmid G, Garnier MG, Büttner M, Oelhafen P (2005) Alloy formation of supported gold nanoparticles at their transition from clusters to solids: does size matter? Phys Rev Lett 94:016804
20. Pei Y, Shao N, Gao Y, Zeng XC (2010) Investigating active site of gold nanoparticle $Au_{55}(PPh_3)_{12}Cl_6$ in selective oxidation. ACS Nano 4:2009
21. Turner M, Golovko VB, Vaughan OPH, Abdulkin P, Berenguer-Murcia A, Tikhov MS, Johnson BFG, Lambert RM (2008) Selective oxidation with dioxygen by gold nanoparticle catalysts derived from 55-atom clusters. Nature 454:981
22. Pan Y, Leifert A, Ruau D, Neuss S, Bornemann J, Schmid G, Brandau W, Simon U, Jahnen-Dechent W (2009) Gold nanoparticles of diameter 1.4 nm trigger necrosis by oxidative stress and mitochondrial damage. Small 5:2067
23. Smith BA, Zhang JZ, Giebel U, Schmid G (1997) Direct probe of size-dependent electronic relaxation in single-sized Au and nearly monodisperse Pt colloidal nano-particles. Chem Phys Lett 270:139
24. Schmid G, Klein N, Korste L, Kreibig U, Schönauer D (1988) Large transition metal clusters—VI. Ligand exchange reactions on $Au_{55}(PPh_3)_{12}Cl_6$—the formation of a water soluble Au_{55} cluster. Polyhedron 7:605
25. Saha K, Bajaj A, Duncan B, Rotello VM (2011) Beauty is skin deep: a surface monolayer perspective on nanoparticle interactions with cells and bio-macromolecules. Small 7:1903
26. Schmid G (1985) Developments in transition metal cluster chemistry — the way to large clusters. Struct Bond 62:51

27. Cho W-S, Cho M, Jeong J, Choi M, Cho H-Y, Han BS, Kim SH, Kim HO, Lim YT, Chung BH, Jeong J (2009) Acute toxicity and pharmacokinetics of 13 nm-sized PEG-coated gold nanoparticles. Toxicol Appl Pharmacol 236:16
28. Li JJ, Hartono D, Ong C-N, Bay B-H, Yung L-YL (2010) Autophagy and oxidative stress associated with gold nanoparticles. Biomaterials 31:5996
29. Johnston HJ, Hutchison G, Christensen FM, Peters S, Hankin S, Stone V (2010) A review of the in vivo and in vitro toxicity of silver and gold particulates: particle attributes and biological mechanisms responsible for the observed toxicity. Crit Rev Toxicol 40:328
30. Shang L, Brandholt S, Stockmar F, Trouillet V, Bruns M, Nienhaus GU (2012) Effect of protein adsorption on the fluorescence of ultrasmall gold nanoclusters. Small 8:661
31. De Paoli Lacerda SH, Park JJ, Meuse C, Pristinski D, Becker ML, Karim A, Douglas JF (2010) Interaction of gold nanoparticles with common human blood proteins. ACS Nano 4:365
32. Treuel L, Nienhaus GU (2012) Toward a molecular understanding of nanoparticle–protein interactions. Biophys Rev 4:137
33. Dhar S, Daniel WL, Giljohann DA, Mirkin CA, Lippard SJ (2009) Polyvalent oligonucleotide gold nanoparticle conjugates as delivery vehicles for Platinum(IV) warheads. J Am Chem Soc 131:14652
34. Rosi NL, Mirkin CA (2005) Nanostructures in biodiagnostics. Chem Rev 105:1547
35. Elghanian R, Storhoff JJ, Mucic RC, Letsinger RL, Mirkin CA (1997) Selective colorimetric detection of polynucleotides based on the distance-dependent optical properties of gold nanoparticles. Science 277:1078
36. Storhoff JJ, Elghanian R, Mucic RC, Mirkin CA, Letsinger RL (1998) One-pot colorimetric differentiation of polynucleotides with single base imperfections using gold nanoparticle probes. J Am Chem Soc 120:1959
37. Storhoff JJ, Lazarides AA, Mucic RC, Mirkin CA, Letsinger RL, Schatz GC (2000) What controls the optical properties of DNA-linked gold nanoparticle assemblies? J Am Chem Soc 122:4640
38. Mucic RC, Storhoff JJ, Mirkin CA, Letsinger RL (1998) DNA-directed synthesis of binary nanoparticle network materials. J Am Chem Soc 120:12674
39. Taton TA, Lu G, Mirkin CA (2001) Two-color labeling of oligonucleotide arrays via size-selective scattering of nanoparticle probes. J Am Chem Soc 123:5164
40. Rosi NL, Giljohann DA, Thaxton CS, Lytton-Jean AKR, Han MS, Mirkin CA (2006) Oligonucleotide-modified gold nanoparticles for intracellular gene regulation. Science 312:1027
41. Seferos DS, Giljohann DA, Hill HD, Prigodich AE, Mirkin CA (2007) Nano-flares: probes for transfection and mRNA detection in living cells. J Am Chem Soc 129:15477
42. Demers LM, Mirkin CA, Mucic RC, Reynolds RA, Letsinger RL, Elghanian R, Viswanadham G (2000) A fluorescence-based method for determining the surface coverage and hybridization efficiency of thiol-capped oligonucleotides bound to gold thin films and nanoparticles. Anal Chem 72:5535
43. Jin R, Wu G, Li Z, Mirkin CA, Schatz GC (2003) What controls the melting properties of DNA-linked gold nanoparticle assemblies? J Am Chem Soc 125:1643
44. Giljohann DA, Seferos DS, Prigodich AE, Patel PC, Mirkin CA (2009) Gene regulation with polyvalent siRNA-nanoparticle conjugates. J Am Chem Soc 131:2072
45. Mirkin CA, Letsinger RL, Mucic RC, Storhoff JJ (1996) A DNA-based method for rationally assembling nanoparticles into macroscopic materials. Nature 382:607
46. Nam J-M, Park S-J, Mirkin CA (2002) Bio-barcodes based on oligonucleotide-modified nanoparticles. J Am Chem Soc 124:3820
47. Park S-J, Lazarides AA, Mirkin CA, Brazis PW, Kannewurf CR, Letsinger RL (2000) The electrical properties of gold nanoparticle assemblies linked by DNA. Angew Chem Int Ed 39:3845

48. Taton TA, Mucic RC, Mirkin CA, Letsinger RL (2000) The DNA-mediated formation of supramolecular mono- and multilayered nanoparticle structures. J Am Chem Soc 122:6305
49. Cutler JI, Auyeung E, Mirkin CA (2012) Spherical nucleic acids. J Am Chem Soc 134:1376
50. Lee J-S, Han MS, Mirkin CA (2007) Colorimetric detection of mercuric ion (Hg^{2+}) in aqueous media using DNA-functionalized gold nanoparticles. Angew Chem Int Ed 46:4093
51. Zheng G, Daniel WL, Mirkin CA (2008) A new approach to amplified telomerase detection with polyvalent oligonucleotide nanoparticle conjugates. J Am Chem Soc 130:9644
52. Han MS, Lytton-Jean AKR, Oh B-K, Heo J, Mirkin CA (2006) Colorimetric screening of DNA-binding molecules with gold nanoparticle probes. Angew Chem Int Ed 45:1807
53. Xu X, Daniel WL, Wei W, Mirkin CA (2010) Colorimetric Cu^{2+} detection using DNA-modified gold-nanoparticle aggregates as probes and click chemistry. Small 6:623
54. Lytton-Jean AKR, Mirkin CA (2005) A thermodynamic investigation into the binding properties of DNA functionalized gold nanoparticle probes and molecular fluorophore probes. J Am Chem Soc 127:12754
55. Seferos DS, Prigodich AE, Giljohann DA, Patel PC, Mirkin CA (2009) Polyvalent DNA nanoparticle conjugates stabilize nucleic acids. Nano Lett 9:308
56. Giljohann DA, Seferos DS, Patel PC, Millstone JE, Rosi NL, Mirkin CA (2007) Oligonucleotide loading determines cellular uptake of DNA-modified gold nanoparticles. Nano Lett 7:3818
57. Cutler JI, Zhang K, Zheng D, Auyeung E, Prigodich AE, Mirkin CA (2011) Polyvalent nucleic acid nanostructures. J Am Chem Soc 133:9254
58. Patel PC, Giljohann DA, Daniel WL, Zheng D, Prigodich AE, Mirkin CA (2010) Scavenger receptors mediate cellular uptake of polyvalent oligonucleotide-functionalized gold nanoparticles. Bioconjugate Chem 21:2250
59. Cutler JI, Zheng D, Xu X, Giljohann DA, Mirkin CA (2010) Polyvalent oligonucleotide iron oxide nanoparticle "click" conjugates. Nano Lett 10:1477
60. Witten KG, Rech C, Eckert T, Charrak S, Richtering W, Elling L, Simon U (2011) Glyco-DNA–gold nanoparticles: lectin-mediated assembly and dual-stimuli response. Small 7:1954
61. van Kasteren SI, Campbell SJ, Serres S, Anthony DC, Sibson NR, Davis BG (2009) Glyconanoparticles allow pre-symptomatic in vivo imaging of brain disease. Proc Natl Acad Sci USA 106:18
62. Ebisu S, Shankar Iyer PN, Goldstein IJ (1978) Equilibrium dialysis and carbohydrate-binding studies on the 2-acetamido-2-deoxy-d-glucopyranosyl-binding lectin from *Bandeiraea simplicifolia* seeds. Carbohydr Res 61:129
63. Zook JM, Long SE, Cleveland D, Geronimo CLA, MacCuspie RI (2011) Measuring silver nanoparticle dissolution in complex biological and environmental matrices using UV–visible absorbance. Anal Bioanal Chem 401:1993
64. Kittler S, Greulich C, Diendorf J, Köller M, Epple M (2010) Toxicity of silver nanoparticles increases during storage because of slow dissolution under release of silver ions. Chem Mater 22:4548
65. Ho C-M, Yau SK-W, Lok C-N, So M-H, Che C-M (2010) Oxidative dissolution of silver nanoparticles by biologically relevant oxidants: a kinetic and mechanistic study. Chem Asian J 5:285
66. Liu J, Hurt RH (2010) Ion release kinetics and particle persistence in aqueous nano-silver colloids. Environ Sci Technol 44:2169
67. Liu J, Sonshine DA, Shervani S, Hurt RH (2010) Controlled release of biologically active silver from nanosilver surfaces. ACS Nano 4:6903
68. Zhang W, Yao Y, Sullivan N, Chen Y (2011) Modeling the primary size effects of citrate-coated silver nanoparticles on their ion release kinetics. Environ Sci Technol 45:4422
69. Braydich-Stolle L, Hussain S, Schlager JJ, Hofmann M-C (2005) In vitro cytotoxicity of nanoparticles in mammalian germline stem cells. Toxicol Sci 88:412

70. Soto K, Carrasco A, Powell TG, Garza KM, Murr L (2005) Comparative in vitro cytotoxicity assessment of some manufactured nanoparticulate materials characterized by transmission-electron microscopy. J Nanopart Res 7:145
71. Foldbjerg R, Dang DA, Autrup H (2011) Cytotoxicity and genotoxicity of silver nanoparticles in the human lung cancer cell line, A549. Arch Toxicol 85:743
72. Benn TM, Westerhoff P (2008) Nanoparticle silver released into water from commercially available sock fabrics. Environ Sci Technol 42:4133
73. Geranio L, Heuberger M, Nowack B (2009) The behavior of silver nanotextiles during washing. Environ Sci Technol 43:8113
74. Navarro E, Piccapietra F, Wagner B, Marconi F, Kaegi R, Odzak N, Sigg L, Behra R (2008) Toxicity of silver nanoparticles to *Chlamydomonas reinhardtii*. Environ Sci Technol 42:8959
75. Kaegi R, Sinnet B, Zuleeg S, Hagendorfer H, Mueller E, Vonbank R, Boller M, Burkhardt M (2010) Release of silver nanoparticles from outdoor facades. Environ Pollut 158:2900
76. Nowack B, Krug HF, Height M (2011) 120 Years of nanosilver history: implications for policy makers. Environ Sci Technol 45:1177
77. Lea MC (1889) Am J Sci 37:476
78. Gottschalk F, Scholz RW, Nowack B (2010) Probabilistic material flow modeling for assessing the environmental exposure to compounds: methodology and an application to engineered nano-TiO_2 particles. Environ Model Softw 25:320
79. Asharani PV, Lianwu Y, Gong Z, Valiyaveettil S (2011) Comparison of the toxicity of silver, gold and platinum nanoparticles in developing zebrafish embryos. Nanotoxicology 5:43
80. Asharani PV, Xinyi N, Hande MP, Valiyaveettil S (2010) DNA damage and p53-mediated growth arrest in human cells treated with platinum nanoparticles. Nanomedicine 5:51
81. Mahl D, Diendorf J, Ristig S, Greulich C, Li Z-A, Farle M, Köller M, Epple M (2012) Silver, gold, and alloyed silver–gold nanoparticles: characterization and comparative cell-biologic action. J Nanopart Res 14:1153
82. Connor EE, Mwamuka J, Gole A, Murphy CJ, Wyatt MD (2005) Gold nanoparticles are taken up by human cells but do not cause acute cytotoxicity. Small 1:325
83. Murphy CJ, Gole AM, Stone JW, Sisco PN, Alkilany AM, Goldsmith EC, Baxter SC (2008) Gold nanoparticles in biology: beyond toxicity to cellular imaging. Acc Chem Res 41:1721
84. Liu Y, Meyer-Zaika W, Franzka S, Schmid G, Tsoli M, Kuhn H (2003) Gold-cluster degradation by the transition of B-DNA into A-DNA and the formation of nanowires. Angew Chem Int Ed 42:2853
85. Tsoli M, Kuhn H, Brandau W, Esche H, Schmid G (2005) Cellular uptake and toxicity of Au_{55} clusters. Small 1:841
86. Pan Y, Neuss S, Leifert A, Fischler M, Wen F, Simon U, Schmid G, Brandau W, Jahnen-Dechent W (2007) Size dependent cytotoxicity of gold nanoparticles. Small 3:1941
87. Leifert A, Pan Y, Kinkeldey A, Schiefer F, Setzler J, Scheel O, Lichtenbeld H, Schmid G, Wenzel W, Jahnen-Dechent W, Simon U (2013) Differential hERG ion channel activity of ultrasmall gold nanoparticles. Proc Natl Acad Sci USA 110:8004
88. Hirn S, Semmler-Behnke M, Schleh C, Wenk A, Lipka J, Schäffler M, Takenaka S, Möller W, Schmid G, Simon U, Kreyling WG (2011) Particle size-dependent and surface charge-dependent biodistribution of gold nanoparticles after intravenous administration. Eur J Pharm Biopharm 77:407
89. Semmler-Behnke M, Kreyling WG, Lipka J, Fertsch S, Wenk A, Takenaka S, Schmid G, Brandau W (2008) Biodistribution of 1.4- and 18-nm gold particles in rats. Small 4:2108
90. Schmid G (2012) Metal nanoparticles: electronic properties, bioresponse, and synthesis. In: Scott RA (ed) Encyclopedia of inorganic and bioinorganic chemistry. Wiley VCH, doi:10.1002/9781119951438.eibc0284.pub2
91. Schleh C, Semmler-Behnke M, Lipka J, Wenk A, Hirn S, Schäffler M, Schmid G, Simon U, Kreyling WG (2012) Size and surface charge of gold nanoparticles determine absorption across intestinal barriers and accumulation in secondary target organs after oral administration. Nanotoxicology 6:36

92. Lin S, Zhao Y, Nel AE, Lin S (2012) Zebrafish: an in vivo model for nano EHS studies. Small. doi:10.1002/smll.201202115
93. George S, Xia T, Rallo R, Zhao Y, Ji Z, Lin S, Wang X, Zhang H, France B, Schoenfeld D, Damoiseaux R, Liu R, Lin S, Bradley KA, Cohen Y, Nel AE (2011) Use of a high-throughput screening approach coupled with in vivo zebrafish embryo screening to develop hazard ranking for engineered nanomaterials. ACS Nano 5:1805
94. Fako VE, Furgeson DY (2009) Zebrafish as a correlative and predictive model for assessing biomaterial nanotoxicity. Adv Drug Deliv Rev 61:478
95. Simmons SO, Fan C-Y, Ramabhadran R (2009) Cellular stress response pathway system as a sentinel ensemble in toxicological screening. Toxicol Sci 111:202
96. Yang L, Kemadjou J, Zinsmeister C, Bauer M, Legradi J, Muller F, Pankratz M, Jakel J, Strahle U (2007) Transcriptional profiling reveals barcode-like toxicogenomic responses in the Zebrafish embryo. Genome Biol 8:R227
97. Harper SL, Carriere JL, Miller JM, Hutchison JE, Maddux BLS, Tanguay RL (2011) Systematic evaluation of nanomaterial toxicity: utility of standardized materials and rapid assays. ACS Nano 5:4688
98. Pan Y, Leifert A, Graf M, Schiefer F, Thoröe-Boveleth S, Broda J, Halloran MC, Hollert H, Laaf D, Simon U, Jahnen-Dechent W (2013) High-sensitivity real-time analysis of nanoparticle toxicity in green fluorescent protein-expressing zebrafish. Small 863
99. Razansky D, Distel M, Vinegoni C, Ma R, Perrimon N, Koster RW, Ntziachristos V (2009) Multispectral opto-acoustic tomography of deep-seated fluorescent proteins in vivo. Nat Photonics 3:412
100. Dreaden EC, Alkilany AM, Huang X, Murphy CJ, El-Sayed MA (2012) The golden age: gold nanoparticles for biomedicine. Chem Soc Rev 41:2740
101. Matsumura Y, Maeda H (1986) A new concept for macromolecular therapeutics in cancer chemotherapy: mechanism of tumoritropic accumulation of proteins and the antitumor agent Smancs. Cancer Res 46:6387
102. Tkachenko AG, Xie H, Coleman D, Glomm W, Ryan J, Anderson MF, Franzen S, Feldheim DL (2003) Multifunctional gold nanoparticle-peptide complexes for nuclear targeting. J Am Chem Soc 125:4700
103. de la Fuente JM, Berry CC (2005) Tat peptide as an efficient molecule to translocate gold nanoparticles into the cell nucleus. Bioconjug Chem 16:1176
104. Chen J, Wang D, Xi J, Au L, Siekkinen A, Warsen A, Li Z-Y, Zhang H, Xia Y, Li X (2007) Immuno gold nanocages with tailored optical properties for targeted photothermal destruction of cancer cells. Nano Lett 7:1318
105. Lu W, Xiong C, Zhang G, Huang Q, Zhang R, Zhang JZ, Li C (2009) Targeted photothermal ablation of murine melanomas with melanocyte-stimulating hormone analog-conjugated hollow gold nanospheres. Clin Cancer Res 15:876
106. Shilo M, Reuveni T, Motiei M, Popovtzer R (2012) Nanoparticles as computed tomography contrast agents: current status and future perspectives. Nanomedicine 7:257
107. Barreto JA, O'Malley W, Kubeil M, Graham B, Stephan H, Spiccia L (2011) Nanomaterials: applications in cancer imaging and therapy. Adv Mater 23:H18
108. Willmann JK, van Bruggen N, Dinkelborg LM, Gambhir SS (2008) Molecular imaging in drug development. Nat Rev Drug Discov 7:591
109. Krause W (2002) Liver specific X-ray contrast agents. Top Curr Chem 222:173
110. Wang H, Zheng L, Guo R, Peng C, Shen M, Shi X, Zhang G (2012) Dendrimer-entrapped gold nanoparticles as potential CT contrast agents for blood pool imaging. Nanoscale Res Lett 7:190
111. Hainfeld JF, Slatkin DN, Focella TM, Smilowitz HM (2006) Gold nanoparticles: a new X-ray contrast agent. Br J Radiol 79:248
112. Kojima C, Umeda Y, Ogawa M, Harada A, Magata Y, Kono K (2010) X-ray computed tomography contrast agents prepared by seeded growth of gold nanoparticles in PEGylated dendrimer. Nanotechnology 21:245104

113. Cai Q-Y, Kim SH, Choi KS, Kim SY, Byun SJ, Kim KW, Park SH, Juhng SK, Yoon K-H (2007) Colloidal gold nanoparticles as a blood-pool contrast agent for X-ray computed tomography in mice. Invest Radiol 42:797
114. Peng C, Wang H, Guo R, Shen M, Cao X, Zhu M, Zhang G, Shi X (2011) Acetylation of dendrimer-entrapped gold nanoparticles: synthesis, stability, and X-ray attenuation properties. J Appl Polym Sci 119:1673
115. Ghann WE, Aras O, Fleiter T, Daniel M-C (2012) Syntheses and characterization of lisinopril-coated gold nanoparticles as highly stable targeted CT contrast agents in cardiovascular diseases. Langmuir 28:10398
116. Peng C, Zheng L, Chen Q, Shen M, Guo R, Wang H, Cao X, Zhang G, Shi X (2012) PEGylated dendrimer-entrapped gold nanoparticles for in vivo blood pool and tumor imaging by computed tomography. Biomaterials 33:1107
117. Wang H, Zheng L, Peng C, Guo R, Shen M, Shi X, Zhang G (2011) Computed tomography imaging of cancer cells using acetylated dendrimer-entrapped gold nanoparticles. Biomaterials 32:2979
118. Reuveni T, Motiei M, Romman Z, Popovtzer A, Popovtzer R (2011) Targeted gold nanoparticles enable molecular CT imaging of cancer: an in vivo study. Int J Nanomedicine 6:2859
119. Chanda N, Kattumuri V, Shukla R, Zambre A, Katti K, Upendran A, Kulkarni RR, Kan P, Fent GM, Casteel SW, Smith CJ, Boote E, Robertson JD, Cutler C, Lever JR, Katti KV, Kannan R (2010) Bombesin functionalized gold nanoparticles show in vitro and in vivo cancer receptor specificity. Proc Natl Acad Sci USA 107:8760
120. Popovtzer R, Agrawal A, Kotov NA, Popovtzer A, Balter J, Carey TE, Kopelman R (2008) Targeted gold nanoparticles enable molecular CT imaging of cancer. Nano Lett 8:4593
121. Aydogan B, Li J, Rajh T, Chaudhary A, Chmura S, Pelizzari C, Wietholt C, Kurtoglu M, Redmond P (2010) AuNP-DG: deoxyglucose-labeled gold nanoparticles as X-ray computed tomography contrast agents for cancer imaging. Mol Imaging Biol 12:463
122. Lijowski M, Caruthers S, Hu G, Zhang H, Scott MJ, Williams T, Erpelding T, Schmieder AH, Kiefer G, Gulyas G, Athey PS, Gaffney PJ, Wickline SA, Lanza GM (2009) High sensitivity: high-resolution SPECT-CT/MR molecular imaging of angiogenesis in the Vx2 model. Invest Radiol 44:15
123. Hainfeld JF, O'Connor MJ, Dilmanian FA, Slatkin DN, Adams DJ, Smilowitz HM (2011) Micro-CT enables microlocalisation and quantification of Her2-targeted gold nanoparticles within tumour regions. Br J Radiol 84:526
124. Kim D, Park S, Lee JH, Jeong YY, Jon S (2007) Antibiofouling polymer-coated gold nanoparticles as a contrast agent for in vivo X-ray computed tomography imaging. J Am Chem Soc 129:7661
125. Xu M, Wang LV (2006) Photoacoustic imaging in biomedicine. Rev Sci Instrum 77:041101
126. Homan K, Mallidi S, Cooley E, Emelianov S (eds) (2011) Combined photoacoustic and ultrasound imaging of metal nanoparticles in vivo. Pan Stanford Publishing Pte. Ltd., Austin
127. Lu W, Huang Q, Ku G, Wen X, Zhou M, Guzatov D, Brecht P, Su R, Oraevsky A, Wang LV, Li C (2010) Photoacoustic imaging of living mouse brain vasculature using hollow gold nanospheres. Biomaterials 31:2617
128. Emelianov SY, Li P-C, O'Donnell M (2009) Photoacoustics for molecular imaging and therapy. Phys Today 62:34
129. Oraevsky AA (2009) Gold and silver nanoparticles as contrast agents for optoacoustic imaging. In: Wang LV (ed) Photoacoustic imaging and spectroscopy. Taylor and Francis, New York
130. Cobley CM, Chen J, Cho EC, Wang LV, Xia Y (2011) Gold nanostructures: a class of multifunctional materials for biomedical applications. Chem Soc Rev 40:44
131. Homberger M, Simon U (2010) On the application potential of gold nanoparticles in nanoelectronics and biomedicine. Phil Trans R Soc A 368:1405

132. Wang Y, Xie X, Wang X, Ku G, Gill KL, O'Neal DP, Stoica G, Wang LV (2004) Photoacoustic tomography of a nanoshell contrast agent in the in vivo rat brain. Nano Lett 4:1689
133. Wang B, Yantsen E, Larson T, Karpiouk AB, Sethuraman S, Su JL, Sokolov K, Emelianov SY (2009) Plasmonic intravascular photoacoustic imaging for detection of macrophages in atherosclerotic plaques. Nano Lett 9:2212
134. Zhang Q, Iwakuma N, Sharma P, Moudgil BM, Wu C, McNeill J, Jiang H, Grobmyer SR (2009) Gold nanoparticles as a contrast agent for in vivo tumor imaging with photoacoustic tomography. Nanotechnology 20:395102
135. Yoon SJ, Mallidi S, Tam JM, Tam JO, Murthy A, Johnston KP, Sokolov KV, Emelianov SY (2010) Utility of biodegradable plasmonic nanoclusters in photoacoustic imaging. Opt Lett 35:3751
136. Agarwal A, Shao X, Rajian JR, Zhang H, Chamberland DL, Kotov NA, Wang X (2011) Dual-mode imaging with radiolabeled gold nanorods. J Biomed Opt 16:051307
137. Olafsson R, Bauer DR, Montilla LG, Witte RS (2010) Real-time, contrast enhanced photoacoustic imaging of cancer in a mouse window chamber. Opt Express 18:18625
138. Chen L-C, Wei C-W, Souris JS, Cheng S-H, Chen C-T, Yang C-S, Li P-C, Lo L-W (2010) Enhanced photoacoustic stability of gold nanorods by silica matrix confinement. J Biomed Opt 15:016010
139. Agarwal A, Huang SW, O'Donnell M, Day KC, Day M, Kotov N, Ashkenazi S (2007) Targeted gold nanorod contrast agent for prostate cancer detection by photoacoustic imaging. J Appl Phys 102:064701
140. Chamberland DL, Agarwal A, Kotov N, Fowlkes JB, Carson PL, Wang X (2008) Photoacoustic tomography of joints aided by an Etanercept-conjugated gold nanoparticle contrast agent—an ex vivo preliminary rat study. Nanotechnology 19:095101
141. Chen Y-S, Frey W, Kim S, Kruizinga P, Homan K, Emelianov S (2011) Silica-coated gold nanorods as photoacoustic signal nanoamplifiers. Nano Lett 11:348
142. Taruttis A, Herzog E, Razansky D, Ntziachristos V (2010) Real-time imaging of cardiovascular dynamics and circulating gold nanorods with multispectral optoacoustic tomography. Opt Express 18:19592
143. Bayer CL, Chen Y-S, Kim S, Mallidi S, Sokolov K, Emelianov S (2011) Multiplex photoacoustic molecular imaging using targeted silica-coated gold nanorods. Biomed Opt Express 2:1828
144. Skrabalak SE, Chen J, Sun Y, Lu X, Au L, Cobley CM, Xia Y (2008) Gold nanocages: synthesis, properties, and applications. Acc Chem Res 41:1587
145. Moon GD, Choi S-W, Cai X, Li W, Cho EC, Jeong U, Wang LV, Xia Y (2011) A new theranostic system based on gold nanocages and phase-change materials with unique features for photoacoustic imaging and controlled release. J Am Chem Soc 133:4762
146. Yang X, Skrabalak SE, Li Z-Y, Xia Y, Wang LV (2007) Photoacoustic tomography of a rat cerebral cortex in vivo with Au nanocages as an optical contrast agent. Nano Lett 7:3798
147. Sokolov K, Follen M, Aaron J, Pavlova I, Malpica A, Lotan R, Richards-Kortum R (2003) Real-time vital optical imaging of precancer using anti-epidermal growth factor receptor antibodies conjugated to gold nanoparticles. Cancer Res 63:1999
148. Aaron J, Nitin N, Travis K, Kumar S, Collier T, Park SY, José-Yacamán M, Coghlan L, Follen M, Richards-Kortum R, Sokolov K (2007) Plasmon resonance coupling of metal nanoparticles for molecular imaging of carcinogenesis in vivo. J Biomed Opt 12:034007
149. Mallidi S, Larson T, Tam J, Joshi PP, Karpiouk A, Sokolov K, Emelianov S (2009) Multiwavelength photoacoustic imaging and plasmon resonance coupling of gold nanoparticles for selective detection of cancer. Nano Lett 9:2825
150. Gutrath BS, Beckmann MF, Buchkremer A, Eckert T, Timper J, Leifert A, Richtering W, Schmitz G, Simon U (2012) Size-dependent multispectral photoacoustic response of solid and hollow gold nanoparticles. Nanotechnology 23:225707

151. Popović Z, Liu W, Chauhan VP, Lee J, Wong C, Greytak AB, Insin N, Nocera DG, Fukumura D, Jain RK, Bawendi MG (2010) A nanoparticle size series for in vivo fluorescence imaging. Angew Chem Int Ed 122:8649
152. Eghtedari M, Oraevsky A, Copland JA, Kotov NA, Conjusteau A, Motamedi M (2007) High sensitivity of in vivo detection of gold nanorods using a laser optoacoustic imaging system. Nano Lett 7:1914
153. Li P-C, Wei C-W, Liao C-K, Chen C-D, Pao K-C, Wang C-RC, Wu Y-N, Shieh D-B (2007) Photoacoustic imaging of multiple targets using gold nanorods. IEEE Trans Ultrason Ferroelectr Freq Control 54:1642
154. Jokerst JV, Cole AJ, Van de Sompel D, Gambhir SS (2012) Gold nanorods for ovarian cancer detection with photoacoustic imaging and resection guidance via raman imaging in living mice. ACS Nano 6:10366
155. Li P-C, Wang C-RC, Shieh D-B, Wei C-W, Liao C-K, Poe C, Jhan S, Ding A-A, Wu Y-N (2008) In vivo photoacoustic molecular imaging with simultaneous multiple selective targeting using antibody-conjugated gold nanorods. Opt Express 16:18605
156. Huang G, Yang S, Yuan Y, Xing D (2011) Combining X-ray and photoacoustics for in vivo tumor imaging with gold nanorods. Appl Phys Lett 99:123701
157. Song KH, Kim C, Cobley CM, Xia Y, Wang LV (2008) Near-infrared gold nanocages as a new class of tracers for photoacoustic sentinel lymph node mapping on a rat model. Nano Lett 9:183
158. Bao C, Beziere N, del Pino P, Pelaz B, Estrada G, Tian F, Ntziachristos V, de la Fuente JM, Cui D (2013) Gold nanoprisms as optoacoustic signal nanoamplifiers for in vivo bioimaging of gastrointestinal cancers. Small 9:68
159. Orendorff CJ, Sau TK, Murphy CJ (2006) Shape-dependent plasmon-resonant gold nanoparticles. Small 2:636
160. El-Sayed MA (2001) Some interesting properties of metals confined in time and nanometer space of different shapes. Acc Chem Res 34:257
161. Alkilany AM, Thompson LB, Boulos SP, Sisco PN, Murphy CJ (2012) Gold nanorods: their potential for photothermal therapeutics and drug delivery, tempered by the complexity of their biological interactions. Adv Drug Deliv Rev 64:190
162. Kreibig U, Vollmer M (1995) Optical properties of metal clusters. Springer, Berlin
163. Skirtach AG, Dejugnat C, Braun D, Susha AS, Rogach AL, Parak WJ, Möhwald H, Sukhorukov GB (2005) The role of metal nanoparticles in remote release of encapsulated materials. Nano Lett 5:1371
164. Chou C-H, Chen C-D, Wang CRC (2005) Highly efficient, wavelength-tunable, gold nanoparticle based optothermal nanoconvertors. J Phys Chem B 109:11135
165. Pissuwan D, Valenzuela SM, Cortie MB (2006) Therapeutic possibilities of plasmonically heated gold nanoparticles. Trends Biotechnol 24:62
166. Pitsillides CM, Joe EK, Wei X, Anderson RR, Lin CP (2003) Selective cell targeting with light-absorbing microparticles and nanoparticles. Biophys J 84:4023
167. Nam J, Won N, Jin H, Chung H, Kim S (2009) pH-Induced aggregation of gold nanoparticles for photothermal cancer therapy. J Am Chem Soc 131:13639
168. Huang X, El-Sayed IH, Qian W, El-Sayed MA (2006) Cancer cell imaging and photothermal therapy in the near-infrared region by using gold nanorods. J Am Chem Soc 128:2115
169. Chen J, McLellan JM, Siekkinen A, Xiong Y, Li Z-Y, Xia Y (2006) Facile synthesis of gold–silver nanocages with controllable pores on the surface. J Am Chem Soc 128:14776
170. Chen J, Glaus C, Laforest R, Zhang Q, Yang M, Gidding M, Welch MJ, Xia Y (2010) Gold nanocages as photothermal transducers for cancer treatment. Small 6:811
171. Au L, Zheng D, Zhou F, Li Z-Y, Li X, Xia Y (2008) A quantitative study on the photothermal effect of immuno gold nanocages targeted to breast cancer cells. ACS Nano 2:1645
172. Hirsch LR, Stafford RJ, Bankson JA, Sershen SR, Rivera B, Price RE, Hazle JD, Halas NJ, West JL (2003) Nanoshell-mediated near-infrared thermal therapy of tumors under magnetic resonance guidance. Proc Natl Acad Sci USA 100:13549

173. Lal S, Clare SE, Halas NJ (2008) Nanoshell-enabled photothermal cancer therapy: impending clinical impact. Acc Chem Res 41:1842
174. O'Neal DP, Hirsch LR, Halas NJ, Payne JD, West JL (2004) Photo-thermal tumor ablation in mice using near infrared-absorbing nanoparticles. Cancer Lett 209:171
175. Loo C, Lowery A, Halas NJ, West J, Drezek R (2005) Immunotargeted nanoshells for integrated cancer imaging and therapy. Nano Lett 5:709
176. Day ES, Zhang L, Thompson PA, Zawaski JA, Kaffes CC, Gaber MW, Blaney SM, West JL (2012) Vascular-targeted photothermal therapy of an orthotopic murine glioma model. Nanomedicine 7:1133
177. Zhou HS, Honma I, Komiyama H, Haus JW (1994) Controlled synthesis and quantum-size effect in gold-coated nanoparticles. Phys Rev B 50:12052
178. Gobin AM, Watkins EM, Quevedo E, Colvin VL, West JL (2010) Near-infrared-resonant gold/gold sulfide nanoparticles as a photothermal cancer therapeutic agent. Small 6:745
179. Hu M, Chen J, Li Z-Y, Au L, Hartland GV, Li X, Marquez M, Xia Y (2006) Gold nanostructures: engineering their plasmonic properties for biomedical applications. Chem Soc Rev 35:1084
180. Murphy CJ, Sau TK, Gole AM, Orendorff CJ, Gao J, Gou L, Hunyadi SE, Li T (2005) Anisotropic metal nanoparticles: synthesis, assembly, and optical applications. J Phys Chem B 109:13857
181. Huang H-C, Yang Y, Nanda A, Koria P, Rege K (2011) Synergistic administration of photothermal therapy and chemotherapy to cancer cells using polypeptide-based degradable plasmonic matrices. Nanomedicine 6:459
182. Norman RS, Stone JW, Gole A, Murphy CJ, Sabo-Attwood TL (2007) Targeted photothermal lysis of the pathogenic bacteria, *Pseudomonas aeruginosa*, with gold nanorods. Nano Lett 8:302
183. Dickerson EB, Dreaden EC, Huang X, El-Sayed IH, Chu H, Pushpanketh S, McDonald JF, El-Sayed MA (2008) Gold nanorod assisted near-infrared plasmonic photothermal therapy (PPTT) of squamous cell carcinoma in mice. Cancer Lett 269:57
184. Choi WI, Kim J-Y, Kang C, Byeon CC, Kim YH, Tae G (2011) Tumor regression in vivo by photothermal therapy based on gold-nanorod-loaded. Functional Nanocarriers. ACS Nano 5:1995
185. Jain PK, Lee KS, El-Sayed IH, El-Sayed MA (2006) Calculated absorption and scattering properties of gold nanoparticles of different size, shape, and composition: applications in biological imaging and biomedicine. J Phys Chem B 110:7238
186. Huang X, Jain PK, El-Sayed IH, El-Sayed MA (2006) Determination of the minimum temperature required for selective photothermal destruction of cancer cells with the use of immunotargeted gold nanoparticles. Photochem Photobiol 82:412
187. von Maltzahn G, Park J-H, Agrawal A, Bandaru NK, Das SK, Sailor MJ, Bhatia SN (2009) Computationally guided photothermal tumor therapy using long-circulating gold nanorod antennas. Cancer Res 69:3892
188. Dreaden EC, Mackey MA, Huang X, Kang B, El-Sayed MA (2011) Beating cancer in multiple ways using nanogold. Chem Soc Rev 40:3391
189. Wood BJ, Ramkaransingh JR, Fojo T, Walther MM, Libutti SK (2002) Percutaneous tumor ablation with radiofrequency. Cancer 94:443
190. Minelli C, Lowe SB, Stevens MM (2010) Engineering nanocomposite materials for cancer therapy. Small 6:2336
191. Arvizo R, Bhattacharya R, Mukherjee P (2010) Gold nanoparticles: opportunities and challenges in nanomedicine. Expert Opin Drug Deliv 7:753
192. Hainfeld JF, Slatkin DN, Smilowitz HM (2004) The use of gold nanoparticles to enhance radiotherapy in mice. Phys Med Biol 49:N309
193. Pradhan AK, Nahar SN, Montenegro M, Yu Y, Zhang HL, Sur C, Mrozik M, Pitzer RM (2009) Resonant X-ray enhancement of the auger effect in high-Z atoms, molecules, and nanoparticles: potential biomedical applications. J Phys Chem A 113:12356

194. Kong T, Zeng J, Wang X, Yang X, Yang J, McQuarrie S, McEwan A, Roa W, Chen J, Xing JZ (2008) Enhancement of radiation cytotoxicity in breast-cancer cells by localized attachment of gold nanoparticles. Small 4:1537
195. Chang M-Y, Shiau A-L, Chen Y-H, Chang C-J, Chen HHW, Wu C-L (2008) Increased apoptotic potential and dose-enhancing effect of gold nanoparticles in combination with single-dose clinical electron beams on tumor-bearing mice. Cancer Sci 99:1479
196. Zhang X, Xing JZ, Chen J, Ko L, Amanie J, Gulavita S, Pervez N, Yee D, Moore R, Roa W (2008) Enhanced radiation sensitivity in prostate cancer by gold-nanoparticles. Clin Invest Med 31:E160
197. Cho SH (2005) Estimation of tumour dose enhancement due to gold nanoparticles during typical radiation treatments: a preliminary Monte Carlo study. Phys Med Biol 50:N163
198. Cho SH, Jones BL, Krishnan S (2009) The dosimetric feasibility of gold nanoparticle-aided radiation therapy (GNRT) via brachytherapy using low-energy gamma-/X-ray sources. Phys Med Biol 54:4889
199. Roeske JC, Nuñez L, Hoggarth M, Labay E, Weichselbaum RR (2007) Characterization of the theorectical radiation dose enhancement from nanoparticles. Technol Cancer Res Treat 6:395
200. Brun E, Sanche L, Sicard-Roselli C (2009) Parameters governing gold nanoparticle X-ray radiosensitization of DNA in solution. Colloids Surf B Biointerfaces 72:128
201. Foley EA, Carter JD, Shan F, Guo T (2005) Enhanced relaxation of nanoparticle-bound supercoiled DNA in X-ray radiation. Chem Commun 3192
202. Butterworth KT, Wyer JA, Brennan-Fournet M, Latimer CJ, Shah MB, Currell FJ, Hirst DG (2008) Variation of strand break yield for plasmid DNA irradiated with high-Z metal nanoparticles. Radiat Res 170:381
203. Rahman WN, Bishara N, Ackerly T, He CF, Jackson P, Wong C, Davidson R, Geso M (2009) Enhancement of radiation effects by gold nanoparticles for superficial radiation therapy. Nanomed Nanotechnol Biol Med 5:136
204. Liu C-J, Wang C-H, Chen S-T, Chen H-H, Leng W-H, Chien C-C, Wang C-L, Kempson IM, Hwu Y, Lai T-C, Hsiao M, Yang C-S, Chen Y-J, Margaritondo G (2010) Enhancement of cell radiation sensitivity by pegylated gold nanoparticles. Phys Med Biol 55:931
205. Roa W, Zhang X, Guo L, Shaw A, Hu X, Xiong Y, Gulavita S, Patel S, Sun X, Chen J, Moore R, Xing JZ (2009) Gold nanoparticle sensitize radiotherapy of prostate cancer cells by regulation of the cell cycle. Nanotechnology 20:375101
206. Polf JC, Bronk LF, Driessen WHP, Arap W, Pasqualini R, Gillin M (2011) Enhanced relative biological effectiveness of proton radiotherapy in tumor cells with internalized gold nanoparticles. Appl Phys Lett 98:193702
207. Hainfeld JF, Dilmanian FA, Zhong Z, Slatkin DN, Kalef-Ezra JA, Smilowitz HM (2010) Gold nanoparticles enhance the radiation therapy of a murine squamous cell carcinoma. Phys Med Biol 55:3045
208. Zheng Y, Sanche L (2009) Gold nanoparticles enhance DNA damage induced by anti-cancer drugs and radiation. Radiat Res 172:114
209. Leung MKK, Chow JCL, Chithrani BD, Lee MJG, Oms B, Jaffray DA (2011) Irradiation of gold nanoparticles by X-rays: Monte Carlo simulation of dose enhancements and the spatial properties of the secondary electrons production. Med Phys 38:624
210. Carter JD, Cheng NN, Qu Y, Suarez GD, Guo T (2007) Nanoscale energy deposition by X-ray absorbing nanostructures. J Phys Chem B 111:11622
211. Zhang S, Gao J, Buchholz T, Wang Z, Salehpour M, Drezek R, Yu T-K (2009) Quantifying tumor-selective radiation dose enhancements using gold nanoparticles: a Monte Carlo simulation study. Biomed Microdevices 11:925
212. Montenegro M, Nahar SN, Pradhan AK, Huang K, Yu Y (2009) Monte Carlo simulations and atomic calculations for Auger processes in biomedical nanotheranostics. J Phys Chem A 113:12364

213. Jones BL, Krishnan S, Cho SH (2010) Estimation of microscopic dose enhancement factor around gold nanoparticles by Monte Carlo calculations. Med Phys 37:3809
214. Sperling RA, Rivera Gil P, Zhang F, Zanella M, Parak WJ (2008) Biological applications of gold nanoparticles. Chem Soc Rev 37:1896
215. Angelatos AS, Radt B, Caruso F (2005) Light-responsive polyelectrolyte/gold nanoparticle microcapsules. J Phys Chem B 109:3071
216. Skirtach AG, Muñoz Javier A, Kreft O, Köhler K, Piera Alberola A, Möhwald H, Parak WJ, Sukhorukov GB (2006) Laser-induced release of encapsulated materials inside living cells. Angew Chem Int Ed 45:4612
217. Vauthier C, Labarre D, Ponchel G (2007) Design aspects of poly(alkylcyanoacrylate) nanoparticles for drug delivery. J Drug Target 15:641
218. Sauer AM, Schlossbauer A, Ruthardt N, Cauda V, Bein T, Bräuchle C (2010) Role of endosomal escape for disulfide-based drug delivery from colloidal mesoporous silica evaluated by live-cell imaging. Nano Lett 10:3684
219. Schloßbauer A, Sauer AM, Cauda V, Schmidt A, Engelke H, Rothbauer U, Zolghadr K, Leonhardt H, Bräuchle C, Bein T (2012) Cascaded photoinduced drug delivery to cells from multifunctional core–shell mesoporous silica. Adv Healthcare Mater 1:316
220. Ruthardt N, Lamb DC, Bräuchle C (2011) Single-particle tracking as a quantitative microscopy-based approach to unravel cell entry mechanisms of viruses and pharmaceutical nanoparticles. Mol Ther 19:1199
221. Gaitzsch J, Appelhans D, Voit B (2012) Responsive polymersome. Nachr Chem 60:1176
222. Brinkhuis RP, Rutjes FPJT, van Hest JCM (2011) Polymeric vesicles in biomedical applications. Polym Chem 2:1449